JOURNAL OF GEOPHYSICAL RESEARCH, VOL. 109, B02408, doi:10.1029/2003JB002412, 2004

Normal fault growth and linkage in the Whakatane Graben, New Zealand, during the last 1.3 Myr

Susanna K. Taylor[1] and Jonathan M. Bull
School of Ocean and Earth Science, Southampton Oceanography Centre, Southampton, UK

Geoffroy Lamarche and Philip M. Barnes
National Institute of Water and Atmospheric Research, Wellington, New Zealand

Received 21 January 2003; revised 23 October 2003; accepted 4 December 2003; published 18 February 2004.

[1] Determination of fault growth rates and fault network evolution at timescales from 10^4 to 10^6 years has been hampered by a lack of a well-constrained stratigraphic succession that provides a high-fidelity record of fault development over these time periods. Here we show how seismic reflection data of different spatial resolutions can be used to constrain the linkage history and displacement rate variations of a single major fault. We present data collected in the offshore Whakatane Graben, Bay of Plenty, New Zealand, where intense normal faulting occurs as a result of active back extension. The focus of our study is the Rangitaiki Fault, a linked segmented normal fault which is the dominant active structure in the graben. The total linked fault length is ∼20 km and has a displacement of up to 830 ± 130 m in the top 1.5 km of sediments. The fault has been actively growing for the last 1.34 ± 0.51 Myr and has developed from isolated fault segments to a fully linked fault system. Initially, the dominant process of fault growth was tip propagation, with an average and maximum displacement rates of 0.52 ± 0.18 and 0.72 ± 0.23 mm yr^{-1}, respectively. Interaction and linkage became more significant as the fault segments grew toward each other, resulting in the fault network becoming fully linked between 300 and 18 ka. Following fault segment linkages, the average displacement rate of the fault network increased by almost threefold to 1.41 ± 0.31 mm yr^{-1}, while the maximum displacement rate increased to 3.4 ± 0.2 mm yr^{-1}. This is the first time that the growth rate of unlinked fault segments has been resolved and has been shown to be slower than in the subsequent linked fault system. *INDEX TERMS:* 3022 Marine Geology and Geophysics: Marine sediments—processes and transport; 3025 Marine Geology and Geophysics: Marine seismics (0935); 8107 Tectonophysics: Continental neotectonics; 8109 Tectonophysics: Continental tectonics—extensional (0905); 8110 Tectonophysics: Continental tectonics—general (0905); *KEYWORDS:* neotectonics, normal faulting, fault growth

Citation: Taylor, S. K., J. M. Bull, G. Lamarche, and P. M. Barnes (2004), Normal fault growth and linkage in the Whakatane Graben, New Zealand, during the last 1.3 Myr, *J. Geophys. Res.*, *109*, B02408, doi:10.1029/2003JB002412.

1. Introduction

[2] Geological faults develop over long time periods, ∼10^6 years, but variations in the mechanics and kinematics of faulting are poorly constrained over their history. Seismology and geodetic studies provide detailed information on coseismic displacements and aspects of the "seismic cycle," ∼10^2 years. Paleoseismology and longer-term geodetic information may constrain fault movements over several thousand years, but this is very short compared to the timescale of geological processes. The key problem is to integrate these different types of data to understand how fault systems develop through time. Because structural features formed in evolving fault systems, e.g., relays, breached relays, transfer faults, and overlaps [e.g., *Childs et al.*, 1995; *Peacock et al.*, 2000] are essentially temporary, the study of these features is best addressed in recently active or neotectonic fault systems where temporal constraints are available over periods ranging from 10^2 to 10^6 years. Understanding the detailed planform of fault systems through time will aid the development of rupture segmentation models and help constrain earthquake hazard.

[3] There are two main mechanisms for fault growth: tip growth and segment linkage. The first mechanism considers that fault grow by a process of tip propagation in which the rupture dimensions for each slip event depends on the size of the earthquake and the length of the fault [*Walsh and Waterson*, 1988; *Cowie and Scholz*, 1992a, 1992b]. Most models of isolated faults suggest that the slip is a maximum at the center of the fault and decreases to zero at the fault tips with a variety of displacement profiles proposed [e.g.,

---

[1] Now at Fault Analysis Group, University College Dublin, Dublin, Ireland.

0148-0227/04/2003JB002412$09.00

Pollard and Segall, 1987; *Cowie and Scholz*, 1992a; *Burgmann et al.*, 1994]. The second mechanism comprises propagation, interaction, and linkage of segments [*Peacock and Sanderson*, 1991, 1994; *Trudgill and Cartwright*, 1994; *Cartwright et al.*, 1995, 1996]. Linkage provides a mechanism for developing large faults (by coalescing the small faults that nucleate) and localizing the deformation after only a few percent strain. The dominant process of fault growth plus the rate of growth will affect basin geometry and drainage patterns and thus sedimentary facies and sediment accumulation rates [e.g., *Cowie et al.*, 2000]. The fieldwork of *Wu and Bruhn* [1994] and *Cartwright et al.* [1995] in Utah has shown that fault linkage may be a dominant mechanism, at least in simple, low-strain settings. Poor temporal constraints on these data mean that the timescales over which these processes occur, and the variations in fault displacement rates that result are poorly defined.

[4] The elucidation of fault behavior on timescales of 10^4 to 10^6 years requires an area with good stratigraphic resolution, both vertically and along fault strike, which most commonly occurs where the fault system is youthful and active, and sediments record the displacement history. In particular, to faithfully record normal fault development three factors are critical: (1) the sedimentation rate must be of the same order of magnitude as the dip-slip rate on the faults; (2) the sedimentary history must contain identifiable horizons or surfaces whose date of formation is well constrained; and (3) it must be possible to correlate horizons across the fault from hanging wall to footwall.

[5] The Whakatane Graben, the offshore continuation of the Taupo Volcanic Zone, New Zealand (Figure 1), has an exceptionally well developed array of normal faults widely distributed over the graben that meets these criteria and is amenable to study using high-resolution seismic reflection surveying and sediment coring. Seismic reflection experiments were conducted in 1999 (multichannel seismic) and 2001 (single-channel chirp and boomer) over an active fault in the graben, providing a set of closely spaced seismic profiles of differing vertical resolutions. The aim of this paper is to use a long timescale history of fault array development to place temporal constraints on models of fault growth. We integrate the two sets of pseudo-three-dimensional (3-D) seismic data to document the full spatial and temporal development of a central part of the Whakatane Graben, where we identified several fault strand terminations and relays within a thick late Pleistocene sequence. The focus of this paper is the development of the Rangitaiki Fault system (Figure 1) and the linkage and rate of growth of its central segments. This fault is the main structural element of the central part of the graben, as shown by the largest measured displacement within the graben and a maximum vertical slip rate of 2.3 ± 0.5 mm yr^{-1} over the last 18 kyr [*Wright*, 1990]. Furthermore, the Rangitaiki Fault has a hanging wall and footwall stratigraphy that is well imaged on seismic reflection data.

2. Regional Tectonic Setting

[6] The Whakatane Graben is situated in shallow water depths in the Bay of Plenty (Figure 1). The graben is part of the currently active Taupo Fault Belt, which is the youngest rift system within the Taupo Volcanic Zone (TVZ). The TVZ marks the zone of Quaternary back-arc rifting and calc-alkaline volcanism associated with the oblique westward subduction of the Pacific plate beneath the Australian plate at the Hikurangi plate boundary margin [*Walcott*, 1978]. The TVZ has been active for the last 2 Myr, while large caldera forming ignimbrite eruptions have occurred for the last 1.6 Myr [*Houghton et al.*, 1995]. The Whakatane Graben began to subside between 0.6 and 1 Ma [see *Nairn and Beanland*, 1989; *Walcott*, 1984; *Wright*, 1990, 1992; *Davey et al.*, 1995]. Near the Bay of Plenty coast, the extension rate has been estimated to be 12 mm yr^{-1} in a NNW-SSE direction across the full 120 km of the bay [*Walcott*, 1987], although *Nairn and Beanland* [1989] note that the strain is concentrated within the Whakatane Graben. The most recent analysis of geodetic data within the TVZ shows that strain is not homogeneous, and suggests an extension rate of 8 ± 2 mm yr^{-1} for the period 1949–1997 [*Darby et al.*, 2000]. The Whakatane Graben extends some 50 km offshore beneath the continental shelf of the Bay of Plenty from the coastline to the White Island volcano [*Wright*, 1990]. The graben lies in less than 200 m water depth except for deeply incised canyons in the north. Morphologically, the graben is characterized by a 15-km-wide subdued bathymetric trough bounded by the Motuhora scarp to the east and Rurima Ridge, an area of positive relief with back-tilted intensely faulted sediments, to the west.

[7] Seismic reflection data show that the Whakatane Graben is characterized by a 15–20 km wide zone of active normal faulting with shallow subsurface displacements on many faults [*Lamarche et al.*, 2000; *Wright*, 1990]. The graben is filled by approximately 3 km of sediments overlying an irregular basement interpreted as Mesozoic graywackes with volcanic intrusions [*Davey et al.*, 1995]. Structurally the graben is limited to the east by the west dipping White Island Fault and to the west by a diffuse zone of intense faulting on the top of Rurima Ridge. The White Island Fault has a conspicuous seabed expression along the Motuhora scarp, which reaches 80 m in height, and along the White Island canyon. Extensional tectonic structures of the Whakatane Graben extend northward to the base of the continental slope at 36°45′S [*Wright*, 1990]. On the basis of a single multichannel seismic (MCS) reflection profile, *Davey et al.* [1995] postulate that the locus of active deformation has moved eastward with time, and that the most recently formed faults occur in the eastern margin of the Whakatane Graben (Figure 1).

[8] *Wright* [1990] estimated minimum subsidence and extension rates since 18 ka, from 3.5 kHz seismic reflection data acquired across the offshore graben. Subsidence rates range from 0.4 to 3.5 mm yr^{-1}, with an average of ~2 mm yr^{-1} [*Wright*, 1990]. Summation of fault heaves derived from measurements of vertical deformation and assuming a constant fault dip of 45° to 10 km depth indicate a maximum extension rate of 3.5 ± 1.7 mm yr^{-1}. Subsidence within the onshore graben is estimated by *Nairn and Beanland* [1989] and *Beanland et al.* [1990] to be 1–2 mm yr^{-1} since 0.6 Ma, while the western edge has been uplifted at ~1 mm yr^{-1} and the eastern edge has been uplifted by ~0.5 mm yr^{-1}.

[9] The Rangitaiki Fault lies in the center of the graben and extends for ~20 km with a mean orientation of 57°N. The fault runs from 2 km north of Whale Island and ends in a zone of distributed faulting 1.2 km from the White Island

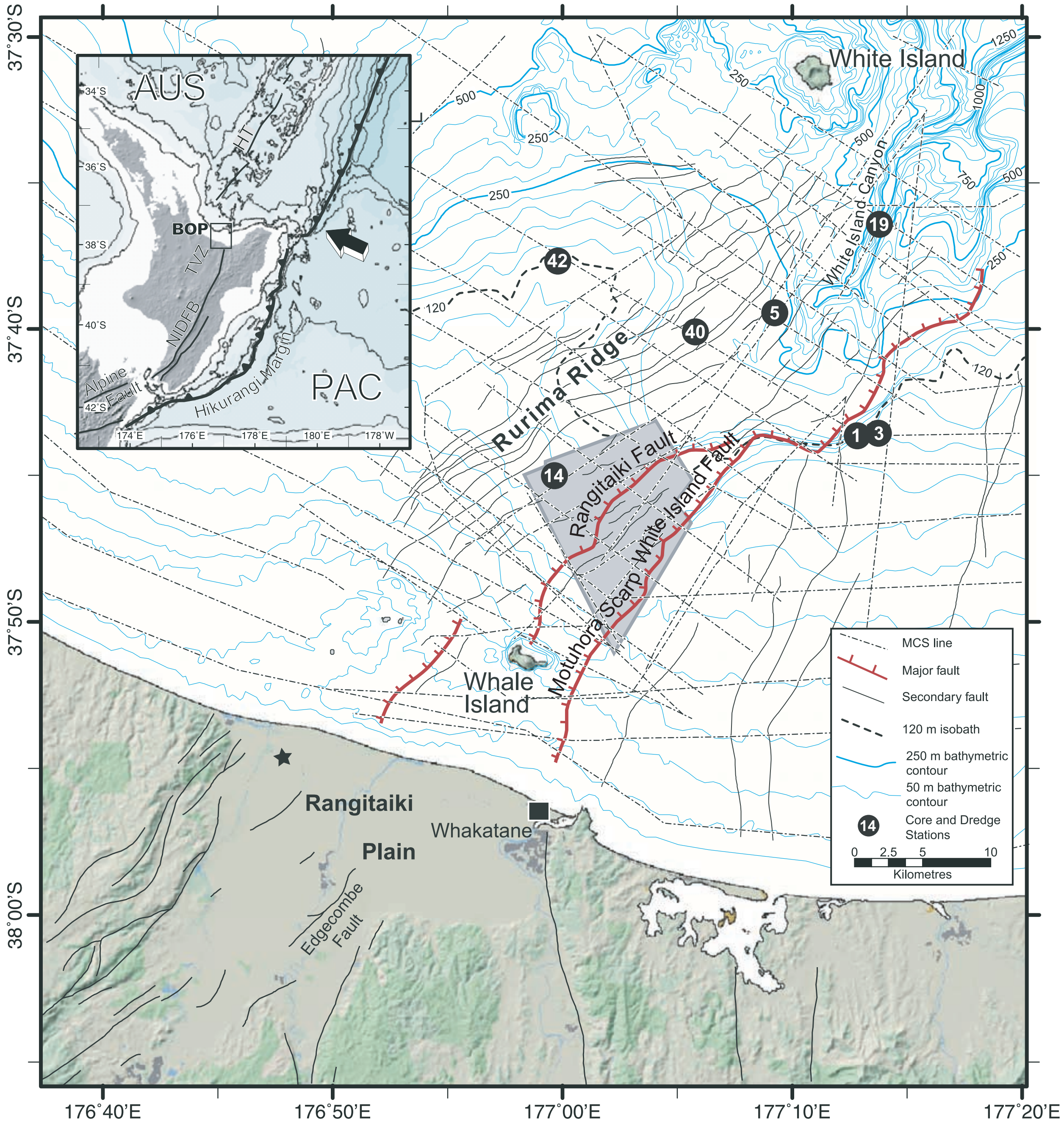

Figure 1. Offshore bathymetric map and onshore digital terrain model of the central Bay of Plenty, with simplified structural features modified from *Wright* [1990], *Lamarche et al.* [2000], and onshore fault database from the Institute of Geological and Nuclear Sciences, New Zealand. Shaded area indicates pseudo-3-D experiment. Star marks the main shock epicenter of the M_L 6.3 Edgecumbe earthquake from *Nairn and Beanland* [1989]. Insert shows geodynamic environment of North Island, New Zealand. Arrow indicates NUVEL-1A PAC-AUS relative plate motion [*De Mets et al.*, 1994]. Bathymetric contour is 500 m. Bold lines indicate major fault systems, NIDBF, North Island Dextral Fault belt; HT, Havre Trough; TVZ, Taupo Volcanic Zone. Teethed line indicates Hikurangi subduction front.

Fault (Figure 1). We identify five active linked segments in the Rangitaiki Fault and resolve the spatial geometry of the fault system.

3. Data Sources

[10] The data used in this study are part of a large data set covering the central Bay of Plenty and the entire offshore Whakatane Graben [*Lamarche et al.*, 2000] and consists largely of multichannel seismic (MCS) air gun and high-resolution single-channel seismic reflection data, as well as a number of shallow core and dredge samples. This data set includes regional seismic profiles and a pseudo-3-D seismic reflection experiment over the central Whakatane Graben, which includes the Rangitaiki Fault. Seismic refraction data were collected to improve velocity control for depth con-

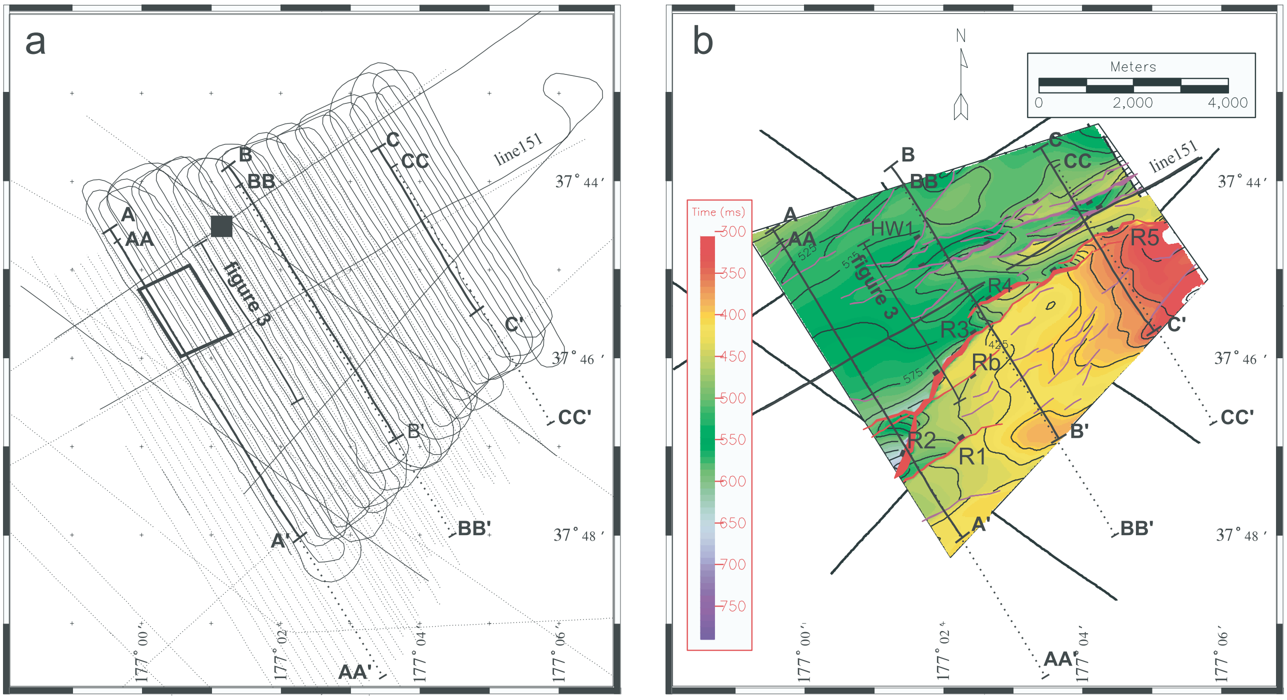

Figure 2. (a) Seismic profiles in the pseudo-3-D survey area. The survey data comprise multichannel seismic profiles and 3.5 kHz profiles (solid lines) and high-resolution chirp and boomer profiles (dotted lines). The survey location is indicated in Figure 1. The refraction sonobuoy was recorded along line 151. The position of multichannel seismic profiles A-A′, B-B′, and C-C′ and high-resolution profiles AA-AA′, BB-BB′, and CC-CC′ illustrated in Figures 6 and 7 are shown. The location of core TAN99-14/14 is shown by the black square. Sediment thickness values from the small boxed area were used in calculating the horizon ages; note that there are no faults in this area. (b) Horizon and structure map of the shallowest horizon interpreted in the multichannel seismic reflection data (MCS1). The position of the profile shown in Figure 3 is highlighted, as are the positions of multichannel seismic profiles A-A′, B-B′, and C-C′, shown in Figures 7. The segmented Rangitaiki Fault is the major fault system running through the area imaged in the multichannel seismic reflection data. Note that the White Island Fault (see Figure 1) is just outside the area, but is imaged in the high-resolution seismic data.

version of the MCS data. The variety of resolutions and penetration enabled us to constrain the evolution of the fault system on timescales of thousands (the top 1–60 m) to millions of years (the top 1.5 km).

[11] This paper focuses on the Rangitaiki Fault and pseudo-3-D survey (Figures 2 and 3), which covers an area of 7.5 × 5 km with seismic profiles 150 m apart. The area was chosen from preliminary shipboard analysis that indicated a well-developed stratigraphy with good potential for recording fault evolution. Excellent quality seismic data were recovered in this area, gas within the sediments was scarce and sufficient water depth limited water bottom multiple interference.

3.1. Multichannel Seismic Reflection Data

[12] The seismic reflection data were collected using a GI gun seismic source and a 48-channel streamer aboard R/V *Tangaroa* in November 1999. The GI gun was used in harmonic mode (75/75 cubic inches), which optimized the peak-to-peak energy ratio [*Pascouet*, 1991], thus combining a high-frequency input signal with sufficient energy to provide high-quality data to a minimum of 1.5 s two-way travel time (TWT).

[13] Data processing included true amplitude recovery, band-pass filter (minimum phase, with corner frequencies of 15, 20, 120, and 150 Hz), predictive deconvolution (operator length 80 ms, predictive distance 8 ms), long-offset mute, normal moveout correction, stack and migration (Kirchoff-Stolt migration using 105% of stacking velocities). The stacked seismic data are 12-fold with a CDP spacing of 6.25 m.

3.2. High-Resolution Seismic Data

[14] The 3.5 kHz seismic reflection profiles were collected in 1999, along with the MCS pseudo-3-D box and regional profiles in the offshore Whakatane Graben. Subsequently, in 2001, 160 km of Chirp subbottom profiler data, 460 km of Boomer subbottom data, and 30 km of side-scan data were acquired aboard R/V *Kaharoa*. Forty-six strike-perpendicular boomer profiles were collected across the Rangitaiki Fault, overlapping the pseudo-3-D box of the R/V *Tangaroa* cruise, although extending farther to the south and east to include the hanging wall sediments of the White Island Fault (Figure 2). These profiles provided information on the top 60 m of sediments. The post-20 ka maps and fault displacement data presented in this paper were derived from the digital boomer data set. The 3.5 kHz and chirp profiles were utilized in improving line-to-line correlation of faults and regional interpretation of stratigraphy.

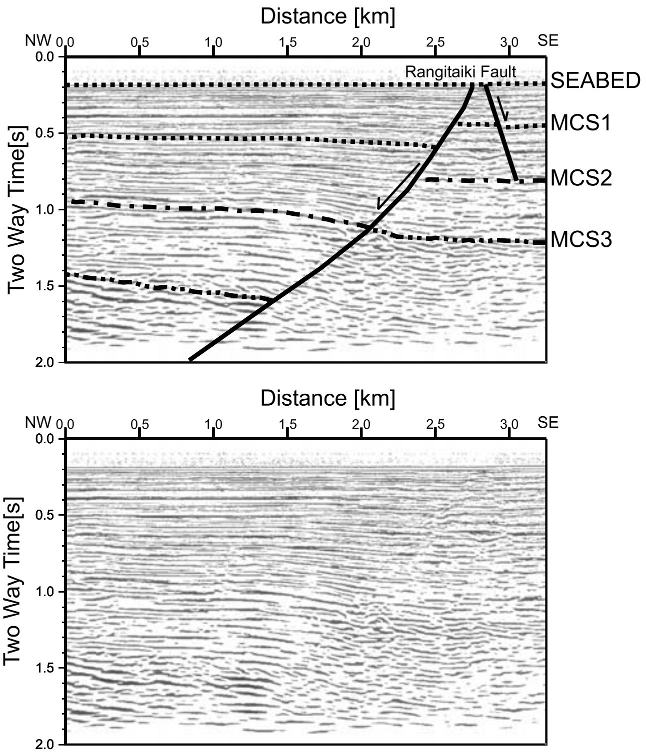

Figure 3. Example of the layered sedimentary sequence imaged by the multichannel seismic data (top, interpreted; bottom, uninterpreted). Location is shown in Figure 2. The Rangitaiki Fault is an extensional growth fault, with no measurable displacement on the MCS data at the seabed. The maximum displacement is generally at horizon MCS3; the highest displacement measured is 830 ± 130 m (this profile). The average dip of the fault is 61°, although this is variable both vertically and along strike. Horizons MCS1 and MCS2 are characterized by on lap above high-amplitude, continuous reflections. Horizon MCS3 is identified by a strong but discontinuous low-frequency reflection associated with a large velocity contrast. The time section is shown at a scale chosen to minimize vertical exaggeration (~1:1 at 2000 m s^{-1}).

[15] Tidal and swell effects are below the resolution of the MCS data, but both the Chirp sonar and Boomer profiles required tide and swell filtering. These filters considerably improve the interpretability of the profiles, and do not affect measurement of fault displacement. The boomer data illustrated in this paper were band-pass-filtered (zero phase, corner frequencies of 300, 1000, 2500, 3000 Hz) following the tidal and swell filtering.

3.3. Sonobuoy Data

[16] One seismic refraction line was recorded using a sonobuoy within the central Whakatane Graben, along line 151 (Figure 2). Three major refracted arrivals could be identified enabling us to construct a 2-D ray-tracing forward model and invert the direct, reflected and refracted arrivals. The model was constructed iteratively downward from the well-constrained velocity profiles of the water column (via an XBT), and near-surface sediments. The interval and layer boundary velocities obtained from the sonobuoy analysis are summarized in Table 1. These values agree well with those from velocity analyses of the MCS reflection data.

3.4. Cores and Dredge Samples

[17] Direct age control consistent with the transgressive sedimentary sequence in the graben is provided by 25 piston cores described by *Kohn and Glasby* [1978] and 18 shallow piston cores collected as part of this project [*Lamarche et al.*, 1999]. Particular reference is made here to Core 14 (Figure 2), which sits within the detailed survey area, and for which age control has been established. The 18 cores collected within the study area were used to derive velocity for the near-surface sediment and to constrain the time-to-depth conversion. The cores, up to 4.5 m long, were split and logged using a whole core geophysical logger [*Best and Gunn*, 1999]. An average interval velocity of 1550 m s^{-1} was found for the relatively uncompacted near-surface sediment within the pseudo-3-D box.

4. Stratigraphic Framework

[18] Sediments within the Whakatane Graben provide a high-fidelity record of fault behavior. In order to constrain the rates at which faults have grown and interacted, we need to understand the stratigraphic framework and age constraints on horizons within the sediment package, which have been used for displacement analysis. The stratigraphy, prominent reflectors imaged and age control of each of the seismic reflection data sets will be considered in turn.

4.1. Deeper Stratigraphy (18 ka to 1.5 Ma)

[19] Three reflectors (MCS1-3) within the MCS profiles collected by the R/V *Tangaroa* could be unambiguously tied around the 3-D box. The overall geometry to 2 s TWT is consistent with a crustal seismic reflection profile across the Bay of Plenty which imaged a variable sedimentary thickness of up to 2.5 s TWT, with "basement" being clearly recognized in places [*Davey et al.*, 1995; *Davey and Lodolo*, 1995]. The sediments are displaced by extensional faults and show thickening into the hanging wall of the fault. The seabed multiple is very low amplitude because of the soft sediment covering the seabed in the graben. Although the total age range of the sedimentary sequence imaged is inferred to be 0–2 Ma from dating of ignimbrites [*Nairn and Beanland*, 1989; *Walcott*, 1984; *Wright*, 1990, 1992; *Davey et al.*, 1995] age control on the reflectors imaged is deduced by extrapolation of near-surface sedimentation rates, and this is now discussed.

Table 1. Velocity Model From Sonobuoy Analysis[a]

Refractor	Layer Depth in Model, m	Interval Velocity, m s^{-1}	Layer Boundary Velocity, m s^{-1} Upper	Layer Boundary Velocity, m s^{-1} Lower	Calculated Two Way Time to Horizon, ms
Sea surface	0	1500 ± 10		1490	0
Seabed	100 ± 10	1715 ± 20	1510	1610	133 ± 10
A	300 ± 30	1925 ± 50	1820	1850	366 ± 40
B	630 ± 60	2160 ± 50	2000	2050	709 ± 82
C	1180 ± 100	2700 ± 100	2270	2400	1218 ± 137

[a] Note that horizons A and C map to MCS1 and MCS 3, but horizon B cannot be reliably associated with MCS2.

[20] Horizon MCS1 is identified as a strong positive and laterally continuous reflector overlying a unit of variable thickness characterized by up to three strong negative peaks. Above horizon MCS1 the overlying sediments onlap (Figure 3, in the hanging wall of the Rangitaiki Fault), although this angular relationship is not well developed on dip sections owing to the regional dip of the seabed. Similarly, horizon MCS2 is defined by a strong reflection with onlapping sediments above (Figure 3).

[21] Horizon MCS3 is defined mainly as a change in seismic character with the seismic attribute becoming noticeably lower frequency (Figure 3), and this coincides with a sharp increase in velocity (Table 1) giving rise to a strong reflector. Figure 3 illustrates a normal faulted block, with the hanging wall strata showing clear syndeformational deposition down to 1.5 s two-way time, above more chaotic low-frequency reflections. There are often diffractions from the tops of the fault blocks on horizon MCS3, although these have been reduced considerably by migration. Horizon MCS3 is interpreted as a change in compacted sedimentary rocks. Dredge and core stations 1, 3, 5, 19, 40, and 42 (Figure 1) from locations where reflections in older sequences are exposed at the seafloor, recovered a range of in situ lithologies including weakly to strongly compacted mudstone and sandstone, carbonate-cemented siliceous lapilli tuff, and indurated and cemented volcanoclastic sediments. In addition, on Whale Island tuffaceous marine sediments separated by lavas, volcanic breccias and slope wash deposits are exposed [*Burt et al.*, 1996], and indicate an inhomogeneous sequence of mudstone and volcaniclastic sediments.

[22] We obtained and dated rock dredge samples from in situ seafloor exposures in order to constrain the age of the multichannel seismic sequence. Dredge samples 5, 19, and 40, from sediments correlated in seismic lines to lie stratigraphically above MCS1, or within 200 ms TWT of this horizon, have been dated biostratigraphically using nannoflora, foraminifera, and palynology, to be of New Zealand Haweran (Wq) stage (<0.34 Ma). Considering the stratigraphic positions of these samples, we infer a conservative age range of 300 ± 100 ka for MCS1 (Table 2). Considering the average depth of MCS1, this age implies an accumulation rate of compacted sediment of 1.05 ± 0.30 mm yr^{-1}. This rate is in broad agreement with the post-18 ka sedimentation rate derived in the following section.

[23] No such biostratigraphic ages are available for the seismic sequence below MCS1. Ages for MCS2 and MCS3 of 770 ± 292 ka and 1340 ± 510 ka, with a 38% error, slightly greater than that associated with the MCS1 age, have been inferred by extrapolating the sediment accumulation rate above MCS1 to the depth converted positions of these horizons (Table 2). The total error on these age estimates includes the uncertainty in velocity, thickness of overlying layers and decompaction. These ages seem reasonable considering the relative stratigraphic positions of the reflectors in the extension graben sequence and the likelihood that much of this sequence developed since inception of back-arc extension about 2 Ma.

Table 2. Age Estimates for the Horizons Interpreted in the MCS Data[a]

Layer	Thickness, ms TWT	Interval Velocity, m s^{-1}	Thickness, m	Age of Base of Layer, a
SEABED-MCS1	367 ± 21	1715 ± 20	315 ± 18	300 ± 100
MCS1-MCS2	513 ± 25	1925 ± 50	493 ± 27	770 ± 292
MCS2-MCS3	556 ± 32	2160 ± 50	601 ± 37	1340 ± 510

[a] Age of MCS1 is constrained by biostratigraphy, while ages for horizons MCS2 and MCS3 are calculated using a 1.05 mm yr^{-1} sedimentation rate (see text). Errors are discussed in the main text.

4.2. Near-Surface Stratigraphy (0–18 ka)

[24] Within the graben there are four strong laterally continuous and easily correlated reflectors in the chirp, boomer and 3.5 kHz data (HRS1-4), which can be used to constrain fault evolution (Figure 4a). Their geometry is summarized in Figure 4b, illustrating the sediment wedge on a strike line up the axis of the Whakatane Graben from the Whale Island platform through the 3-D box. HRS4 overlies an eroded stratigraphy with the wedge of sediments on a strike line north of Whale Island revealing that horizons HRS1-3 progressively onlap HRS4 toward the coast (Figure 4b). The unit between HRS4 and HRS3 thins shoreward, whereas the most recent sediments above HRS1 thicken shoreward. The sequence immediately beneath HRS4 (Figure 4b) dips and progrades to the west.

[25] It is widely recognized [e.g., *Lambeck and Chappell*, 2001] that during the Quaternary, ice ages were times of sea level low stands and interglacials were times of relatively highstands. The New Zealand coastline saw sea level rising from at least 18 ka until 6.5 (±0.1) ka with a notable stillstand from 9.2 to 8.4 ka, and a less significant stillstand from 7.5 to 7.3 ka [*Herzer*, 1981; *Gibb*, 1986; *Carter et al.*, 1986]. *Gibb* [1986] found that during the last 6.5 kyr, sea level has been relatively stable. The coastline of the Rangitaiki Plain was deeply embayed at 6.5 ka and has since prograded at least 10 km with volcaniclastic

Figure 4. (a) Position of core 14 and the four horizons interpreted in the high-resolution seismic data used for measuring fault displacements. Location shown in Figure 4d. Note that HRS4 is picked as the reflector immediately underlying the transparent layer and is interpreted as a transgressive marine ravinement associated with the lowstand maximum (see Figure 4b). The small fault at CDP 560 has a maximum displacement of 9 m at horizon HRS4, and thickening of the syndeformational sediments can be seen in the hanging wall of the fault. Vertical exaggeration is ∼14:1. (b) Schematic of the postglacial wedge on a strike line up the axis of the Whakatane Graben from Whale Island through to the 3-D box (position shown in Figure 4d). The channel system shown would have incised during the last lowstand when the mean elevation of the 3-D box would have been at least 70 m above the lowstand maximum. The channels are preserved because of subsequent rapid episodic transgression over the area. (c) Sea level curve of *Carter et al.* [1986]. The likely age range of HRS4 in the 3-D box is 16–18 ka. Note that sea level rise was episodic. The water depth range in the 3-D box is uncorrected for subsidence. (d) Simplified map showing position of profiles shown in Figures 4a and 4b. The Rangitaiki and White Island Fault systems and the bathymetric contours are in meters.

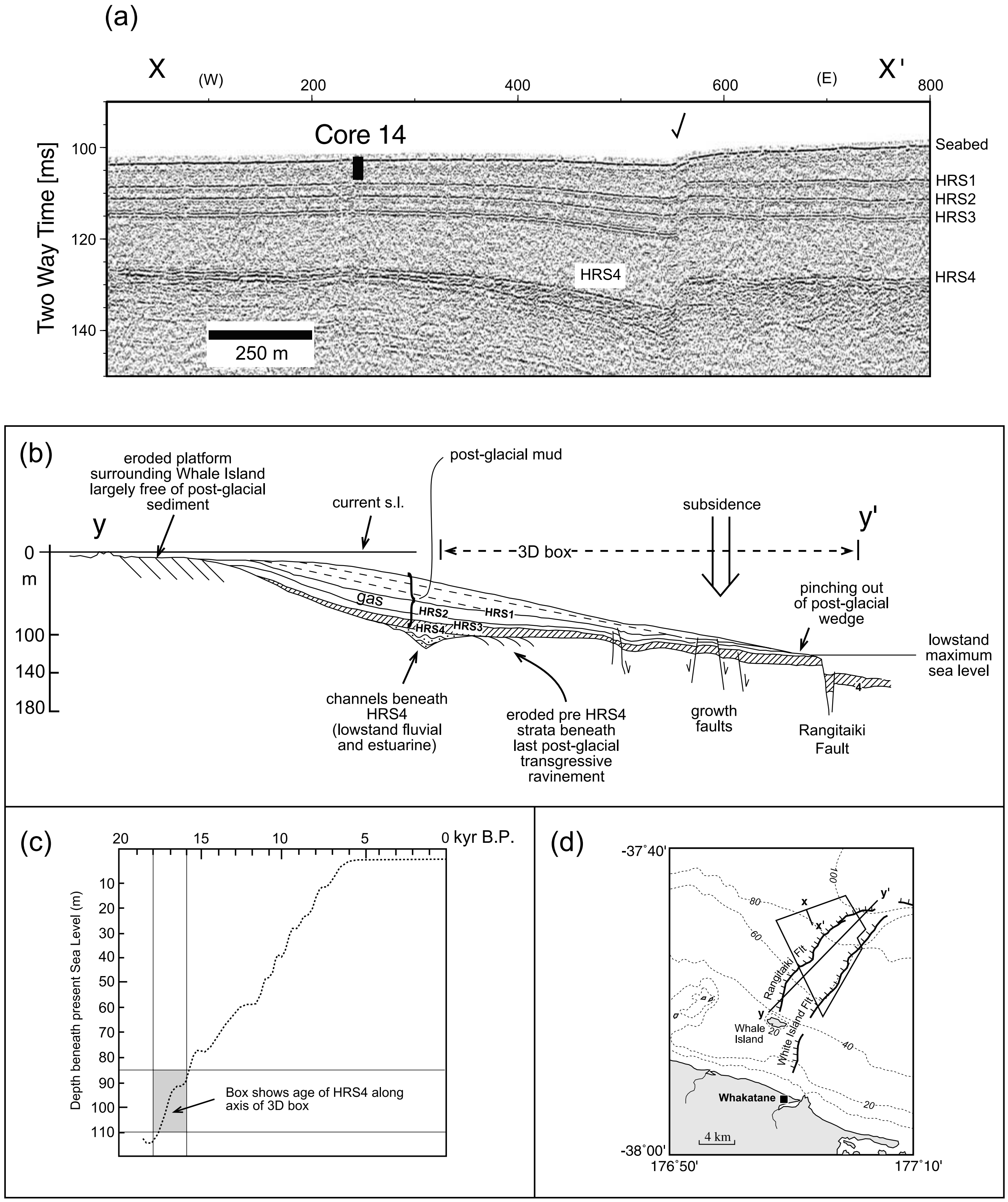
(a)
X
(W)
200
400
600
(E)
X'
800
Core 14
Two Way Time [ms]
100
120
140
250 m
Seabed
HRS1
HRS2
HRS3
HRS4
HRS4
(b)
eroded platform surrounding Whale Island largely free of post-glacial sediment
current s.l.
post-glacial mud
subsidence
y
y'
0
m
100
140
180
3D box
gas
HRS1
HRS2
HRS3
HRS4
pinching out of post-glacial wedge
lowstand maximum sea level
channels beneath HRS4 (lowstand fluvial and estuarine)
eroded pre HRS4 strata beneath last post-glacial transgressive ravinement
growth faults
Rangitaiki Fault
(c)
20
15
10
5
0 kyr B.P.
Depth beneath present Sea Level (m)
10
20
30
40
50
60
70
80
90
100
110
Box shows age of HRS4 along axis of 3D box
(d)
-37˚40'
-38˚00'
176˚50'
177˚10'
x
x'
y
y'
100
80
60
40
20
20
Rangitaiki Flt
White Island Flt
Whale Island
Whakatane
4 km

Figure 4.

sediment supply from major rivers. Notable sedimentation episodes followed the Whakatane, Taupo, and Kaharoa pyroclastic eruptions [*Nairn and Beanland*, 1989; *Beanland and Berryman*, 1992].

[26] The Rangitaiki Fault trace north of Whale Island lies at water depths of 60–100 m (Figure 1). It is to be expected that, at the last sea level lowstand (with sea levels 120–140 m below present), an incising fluvial system would have drained the hinterland to the south within the axis of the subsiding Whakatane Graben. HRS4 is the youngest regionally extensive erosion surface, and likely formed in very shallow water (<20 m) at the low-stand maximum (120–140 m), and diachronously between 120 m and the coast from 18 to 6.5 ka as the zone of marine abrasion moved up. Using the sea level curve of *Carter et al.* [1986] and inferred water depths in the study area near the Rangitaiki Fault at the time of formation of HRS4, we can state that the age of HRS4 in the area relevant to this study is 16–18 ka (Figure 4b). Underlying HRS4, there are clear examples of "nested" channels, which are most likely fluvial systems that fed the Canyon system to the north during the last lowstand. The fact that these fluvial channels are preserved supports sea level rising rapidly over the area of the 3-D box during the formation of HRS4. We cannot rule out a tidal estuarine origin for these systems, however this is not important in terms of assigning an age to HRS4. HRS4 is the transgressive (diachronous) marine ravinement surface, whereas the base of the nested channel fill sequence, whatever its origin, is the true sequence boundary for the last sea level cycle.

[27] Several lines of seismic stratigraphic evidence indicate that the near-surface 5–60 m thick stratigraphic sequence represents the post $\sim$18 ka transgression. First, a series of landward thinning, conformable and onlapping seismic reflectors form the uppermost sedimentary succession that unconformably overlies a strongly reflective horizon, which truncates older stratigraphy. Second, fluvial channels occur near shore beneath the sequence. Third, a stillstand terrace at -109 m immediately east of the graben, which is correlated with the 18 ka stillstand [*Carter et al.*, 1986], conformably underlies an identical, but condensed stratigraphic sequence to that found in the graben. Our estimate of 9 (±1) ka for HRS1 agrees with the previous estimate of 8.5–9.4 ka made by *Wright* [1990]. Underlying the transgressive sequence is HRS4, which as discussed earlier, is interpreted as a transgressive ravinement surface.

[28] Core 14 sediment is a green coarse to fine silty-clay punctuated by distinct coarse-grained ash rich events down the depth (4 m) of the core. Shells at a depth of 2.67 m have a ^{14}C calibrated age of 6856–6609 years B.P. (2002) at the 95% confidence interval. This together with the presence of the Mamaku tephra could be used to constrain the sedimentation rate within the core. At this site the sedimentation rate was less than 0.4 mm yr^{-1} for the last 6.6–6.8 kyr but substantially higher (1.0 mm yr^{-1}, see section 4.1) prior to that. The shallowest reflector used to measure fault displacement offsets (HRS1), is just beneath the base of the core ($\sim$4.2 m), and is consistent with the presence of the primary Mamaku Tephra (7.35 ka [*Froggatt and Lowe*, 1990]) at a depth of 3.40–3.43 m. The lower sedimentation rate for sediments before 6.5 ka can be ascribed to a landward shift in the position of maximum sediment accumulation.

[29] Horizons HRS2 and HRS3 are inferred to be 11.4 (±1) and 13.9 (±1) ka. These ages were derived by taking sediment thicknesses over a 2 km^2 area, indicated in Figure 2a, close to core 14, and interpolating between the inferred ages of the HRS1 (9 ka) and HRS4 (16–18 ka). The area used in the age calculation was chosen because it is close to the site of core 14; relatively unfaulted and is away from the influence of the Rangitaiki Fault, and is representative of the overall stratigraphic framework shown in Figure 4b. The uncertainties in age stated reflect that the HRS4 unconformity is diachronous, but that the water depths within the 3-D box area are relatively uniform (a range of 20 m).

5. Measurements of Fault Displacement

[30] All fault displacement diagrams in this paper are strike projected along a N57°E *x* axis, which corresponds to the average strike of the Rangitaiki Fault. In this projection the *x* axis is referred to as "along strike" and the perpendicular *y* axis as "across strike." This projection displays fault displacements advantageously, and is valuable for comparing faults across strike [e.g., *Childs et al.*, 1993]. Most fault segments within the central Whakatane Graben are only slightly oblique to the *x* axis.

[31] The fault planes exhibit variable dip laterally and vertically, so both the heave and throw components of fault movement are measured, and combined to give the displacement. The difference in displacement on a fault between successive horizons represents the displacement increment in the period between deposition of the two horizons [*Childs et al.*, 1993]. Fault displacement rates for each time period were calculated using the displacement difference between horizons and age estimates of those horizons. The arithmetic means are based on data from a large number of seismic profiles, and the derived values are not influenced by line location.

[32] The closely spaced seismic profiles give excellent coverage of the structure and along-strike displacement variations of the fault. Both displacement and displacement rate are calculated at five locations along strike chosen to correspond to the locations of maximum displacement on the five segments observed in the pseudo-3-D survey area. Maximum displacement values are derived from measurements made on between two and four seismic profiles making them more reliable than single observations of maximum displacement [*Dawers et al.*, 1993].

[33] Errors in the measurement of fault displacements and sediment thickness come from uncertainties in horizon picks, the interval velocities used in-depth conversion and corrections for sediment compaction. Other sources of uncertainty (e.g., acquisition and time migration) are considered negligible (see *Thore et al.* [2002] for a review on error in MCS interpretation). Errors in horizon ages have been previously summarized (Table 2) and range from ±30% for MCS1 to ±38% for MCS2 and MCS3. Errors in the HRS horizon ages are discussed in section 4.2, are lower, and range from 6 to 11%.

[34] Uncertainties in horizon picks are estimated to be one wavelength. The nominal frequency of the data at horizon MCS1 is 70 Hz, reducing to 40 Hz at MCS3. This

equates to ±15 ms at MCS1 and ±25 ms at MCS3. For the high-resolution boomer profiles, an estimated uncertainty of ±0.5 ms is included in each horizon pick. Seismic profiles where the interpretation of the horizons was ambiguous were not included in calculating the fault displacements. The velocity used for depth migration of high-resolution profiles was determined from in situ physical property measurements made on cores collected within the Whakatane Graben, a value of 1550 ± 25 m s^{-1}. Velocities used for depth migration of the MCS horizons were determined from the sonobuoy model using wide-angle reflected and refracted arrivals. The errors derived from inverting the model are shown in Table 1.

[35] Decompaction is performed using the assumption that the change in porosity with depth follows an exponential curve with parameters defined by sediment type [*Sclater and Christie*, 1980]. In the case of growth faulting, displacement is accumulated on a fault while it is being buried, so a proportion of the displacement is accumulated on sediments that have already been compacted. Decompaction of displacements must take into account the displacement that occurred while the horizon was near the surface, which should be decompacted to the surface value of porosity, and displacement that occurred while the horizon is at the depth the measurements were taken at, where no decompaction is required. The effect of varying the parameters of decompaction through a reasonable range for the sediments studied gives a variation in displacement of around 2%. The effect of sedimentary compaction is greatest where the sediments are thickest, the difference between decompacted and compacted fault displacement measurements remains within the estimated uncertainty range for the displacement. In many cases there is some fault drag adjacent to the fault planes observed in both the footwall and the hanging wall. This local perturbation to the displacement fields was corrected for using the technique employed by *Chapman and Meneilly* [1991] and *Mansfield and Cartwright* [1996] whereby the horizons are projected toward the fault plane.

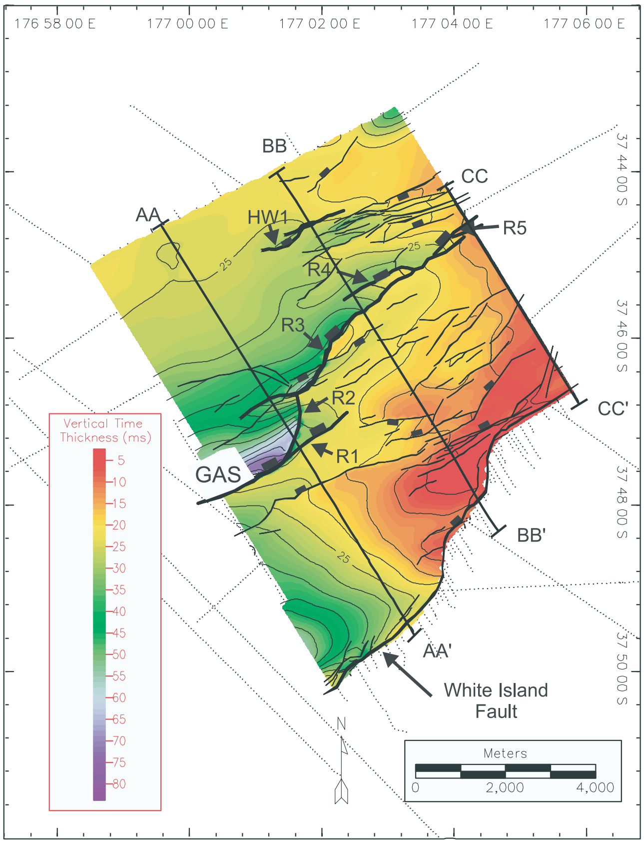

Figure 5. Fault and isopach map of sediments deposited during the last 16–18 kyr derived from high-resolution data shown in Figure 2. The five segments of the Rangitaiki Fault (R1-R5) are shown with clear sediment depocenters in their hanging walls. The White Island fault, which has a scarp at the seabed, is also shown with the center of the sediment depocenter occurring ~1 km away from the fault. See text for more discussion. The positions of the three profiles shown in Figures 6 and 7 are also shown.

6. Results

[36] In this paper we first describe in general terms the structure of the central offshore Whakatane Graben, as interpreted from the 3-D seismic experiment, in order to demonstrate that the Rangitaiki Fault is the main structural feature in the area. We subsequently provide detailed information on the structures of the Rangitaiki Fault from five individual segments to a single linked fault, and finally discuss the processes involved in the evolution of the Rangitaiki Fault, chiefly fault tip propagation and linkage.

6.1. Structural Style in the Whakatane Graben

[37] In all, over eighty fault segments were identified displacing the seven horizons interpreted in the pseudo-3-D seismic survey (Figure 5), the most active, as defined by having the largest Pleistocene and Holocene displacements, are those making up the Rangitaiki Fault and White Island Fault networks. Displacements on horizon HRS4 range from the resolution of the boomer data (50 cm) up to 50 m. The spatial activity of faults within the detailed study area can be illustrated with an isopach map of sedimentation through the last 16–18 kyr (Figure 5). Two main fault systems dominate the area: the Rangitaiki Fault, which is the subject of this paper, and the White Island Fault. The White Island Fault is the dominant fault at the eastern boundary of the Whakatane Graben, and in contrast to the Rangitaiki Fault is not well infilled with sediment and retains a large surface expression throughout the survey area. In addition to the major Rangitaiki and White Island Fault systems, smaller faults displace the sediments in the blocks between. In the hanging wall of the Rangitaiki Fault a graben is formed from a series of normal faults (profile CC-CC′ on Figure 6). Between the Rangitaiki Fault and White Island Fault there are several lower displacement faults, some of these faults form a hanging wall splay at a bend in the White Island Fault (Figure 5).

[38] The thickest accumulation of sediments is found along the Rangitaiki Fault wall. This is in contrast with sediment thickest accumulation found between 300 and 1000 m west of the White Island Fault wall (AA′ on Figure 6a). The positions of three example seismic profiles shown in Figures 6 (high-resolution seismic) and 7 (multichannel seismic) are shown on Figures 5 and 2b, respectively. These seismic profiles show major

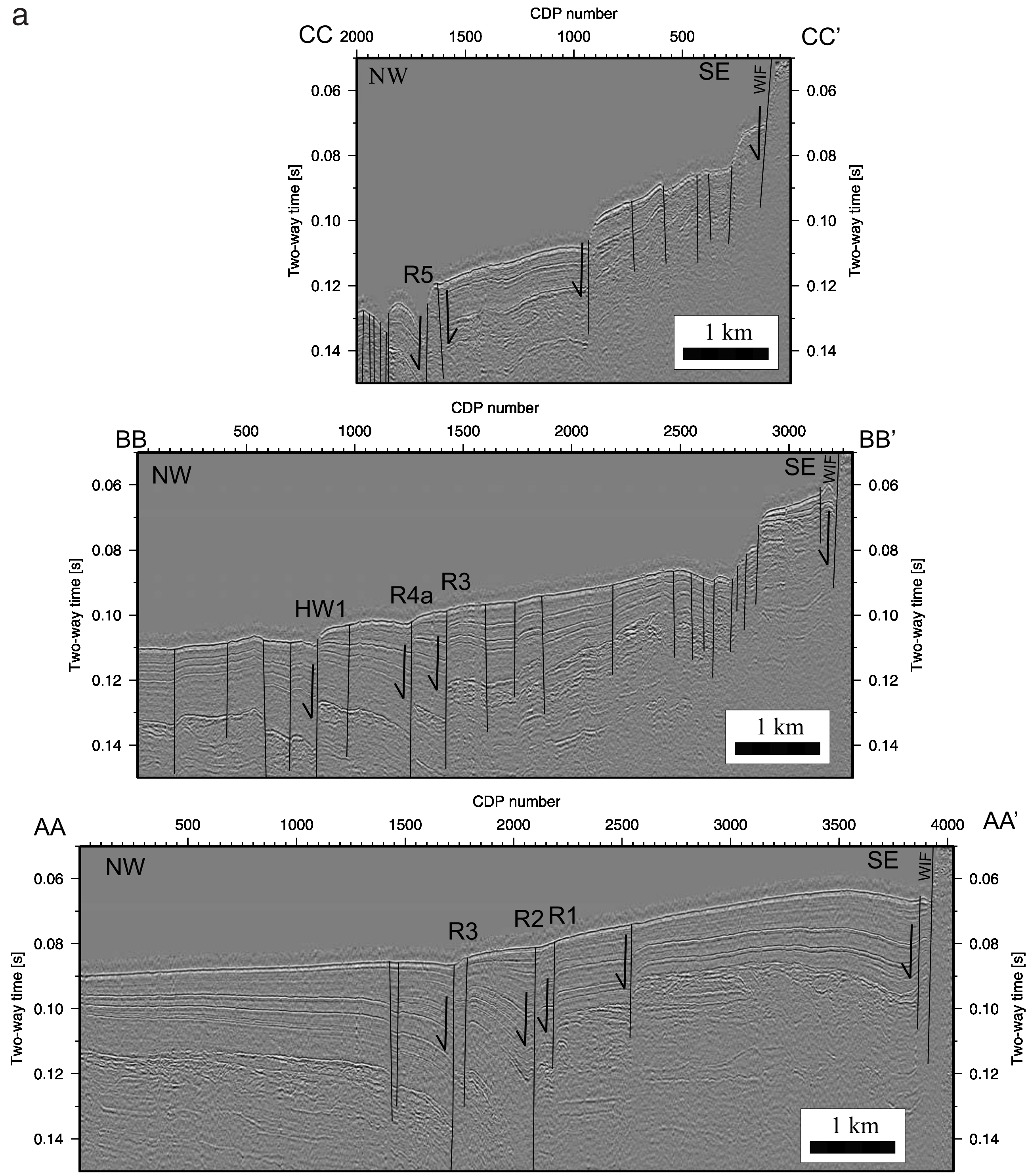

Figure 6. Three example boomer profiles illustrating the Rangitaiki and White Island faults, showing (a) data and (b) interpretation. The locations of profiles AA-AA′, BB-BB′, and CC-CC′ are shown in Figure 2. These profiles image the postglacial sedimentation in the Whakatane Graben (horizons HRS1-4 and a probable fluvial system beneath). Vertical exaggeration is ~45:1.

faults displacing the full thickness of the section, with some smaller faults that are limited in vertical extent. With few exceptions, the faults have been active while the sediments were deposited, shown by thickening of the sediments in the hanging wall and displacement on the faults decreasing upward. The faults have an average dip of 61° ± 2° between horizons MCS1 and MCS3 and gradually increase in dip to 70° to near vertical in the top ~100 m.

[39] In profile A-A′ (Figures 6 and 7), deformation is concentrated on the two major fault systems (Rangitaiki and White Island), with relatively flat lying sediments and

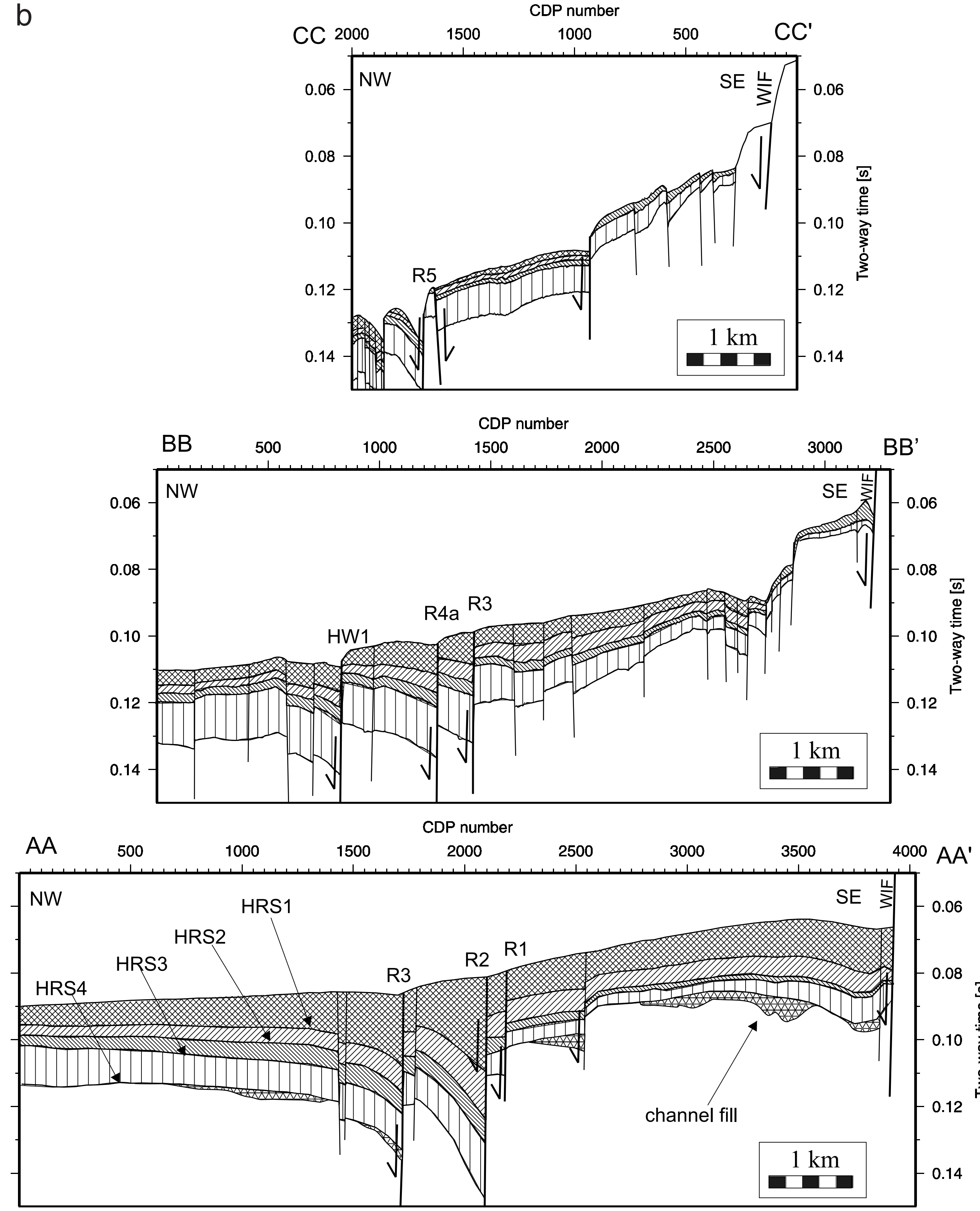

Figure 6. (continued)

very few faults between. In contrast, in the center of the survey area (profile B-B′), the faulting is more evenly distributed through the section and the sediments are tilted into normal fault blocks in the hanging wall of the Rangitaiki Fault. The block-bounding faults are laterally discontinuous, and are not seen in profile C-C′ where the hanging wall of the Rangitaiki Fault is dominated by a collapsed graben.

6.2. Structure of the Rangitaiki Fault

[40] The Rangitaiki Fault comprises five major overlapping and interacting segments (R1, R2, R3, R4, and R5,

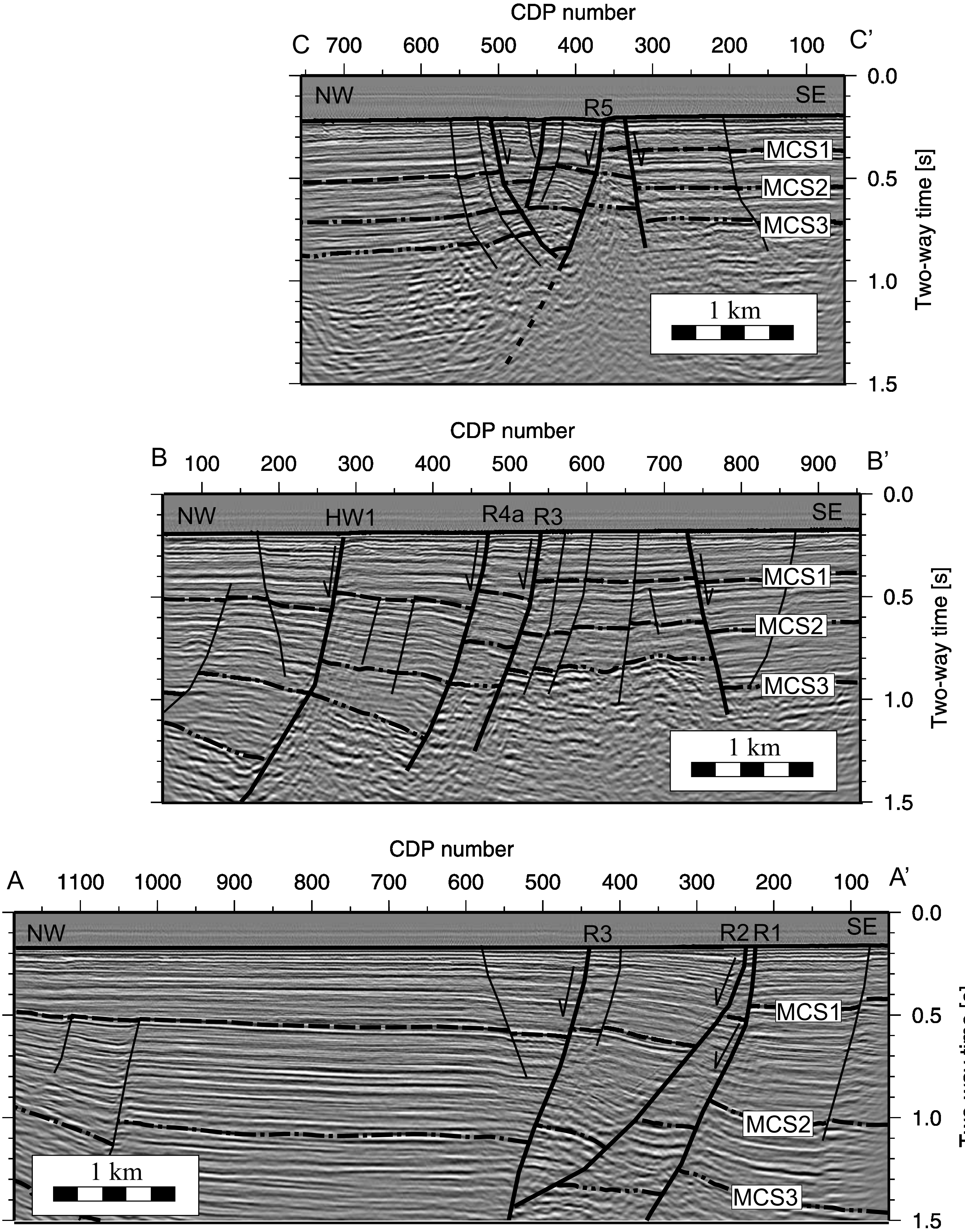

Figure 7. Three example multichannel seismic profiles from the pseudo-3-D survey area illustrating the Rangitaiki Fault displacing horizons MCS1-3. The location of profiles A-A′, B-B′, and C-C′ are shown in Figure 2. The five main segments of the Rangitaiki Fault are indicated with numbers. Profiles show the displacement on the Rangitaiki Fault decreasing and the sedimentary layer thinning by ~50% to the north, toward the tip of the Rangitaiki Fault. Vertical exaggeration is ~2:1 at 2000 m s^{-1}.

Figure 8). Interpretation of regional profiles, suggests no additional segmentation, and allows us to constrain the displacement profile of the Rangitaiki Fault beyond the survey area, albeit in less detail. The regional profiles show the displacement of segments R1 and R5 decreasing away from the detailed survey area toward the fault tips. The maximum displacement observed on the Rangitaiki Fault, within the 3-D box (i.e., not over the whole length of the Rangitaiki Fault) is 830 ± 130 m on the oldest horizon (MCS3) in the center of segment R3 (Figure 9g). Other

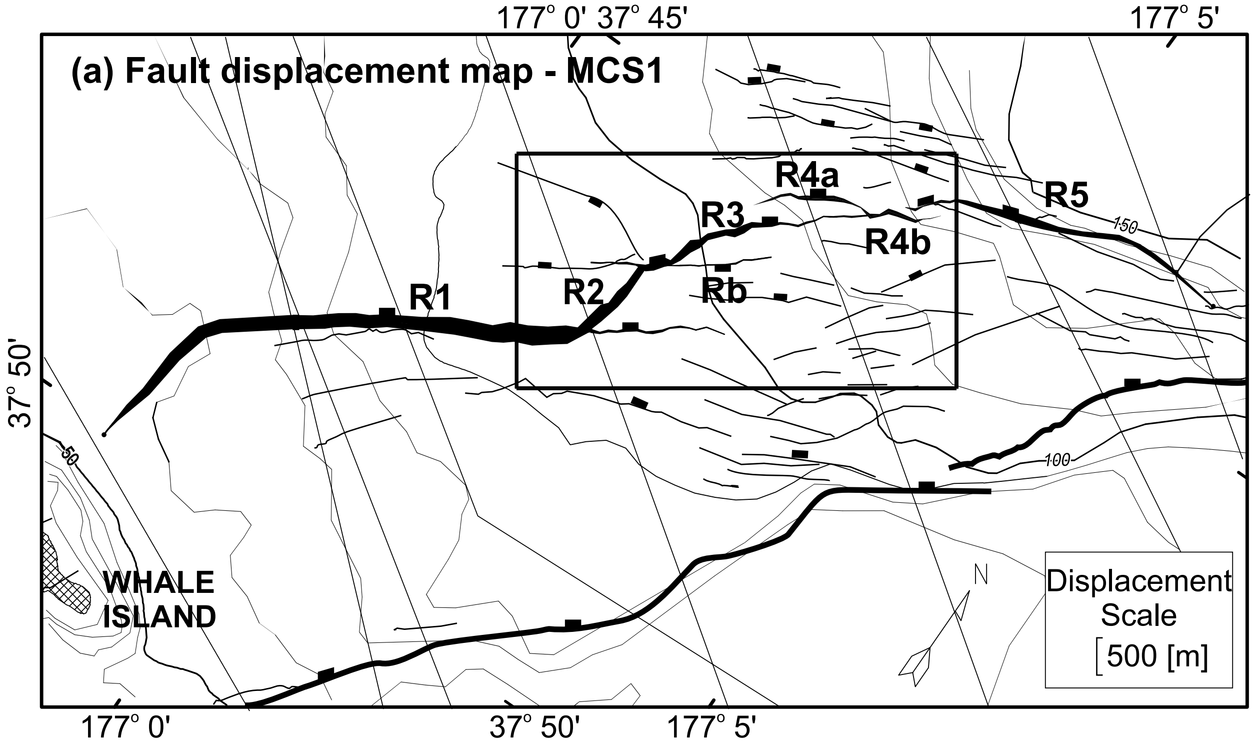

(b) Rangitaiki Fault Displacement Profile - MCS1

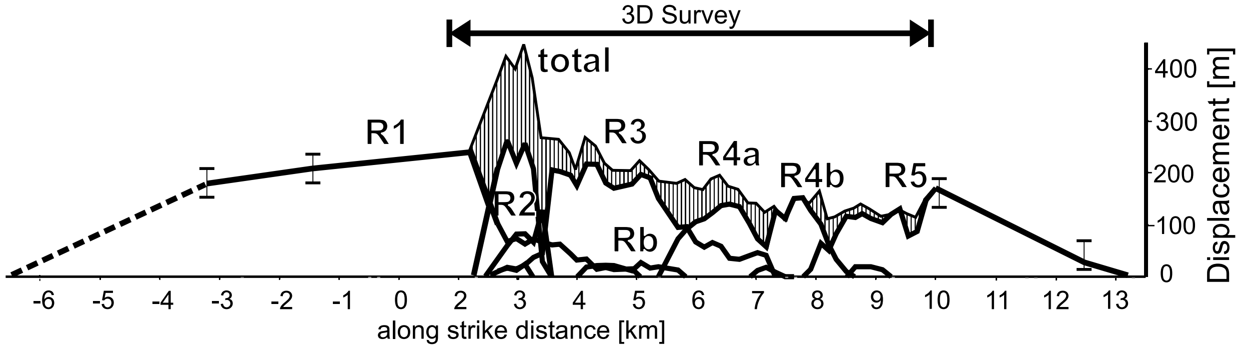

(c) Rangitaiki Fault Displacement Profile - HRS1

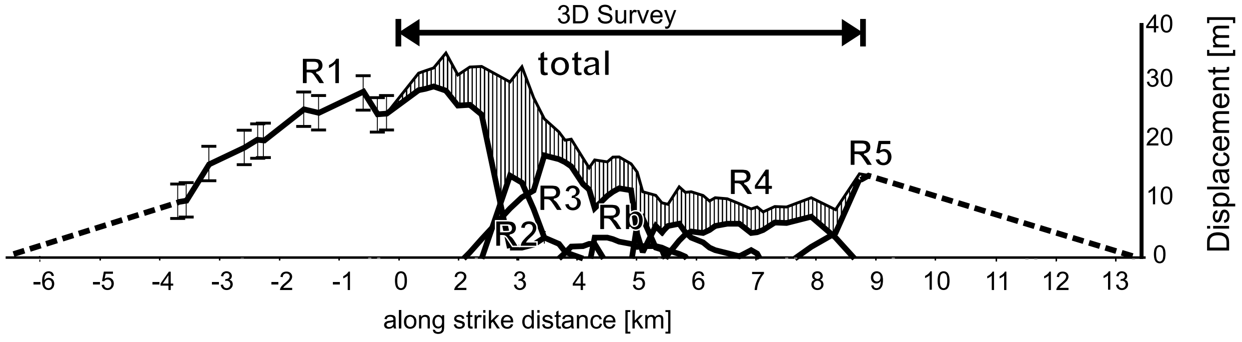

Figure 8.

Rangitaiki Fault segments have maximum displacements of ~300 m. On the younger horizons (MCS1 and MCS2) the maximum displacement is observed on R2 or R1, regional seismic data show that at least on MCS1, the maximum displacement of the entire Rangitaiki Fault lies within the pseudo-3-D survey area.

[41] South of the 3-D box, horizons MCS2 and MCS3 are poorly imaged on the MCS data and horizons HRS2-4 are not imaged in the high-resolution data due to the shallower water depths introducing multiples, and the presence of gas. This affects the southernmost segment, R1, whose evolution is well constrained for the last 300 kyr. For this reason the reconstruction of fault evolution for the Rangitaiki system over 1.3 Myr is only precisely constrained within the 3-D box, and this is the focus of the arguments developed in Figures 9–11. Later (Figure 12) we consider the evolution of the entire Rangitaiki system in general terms.

[42] The displacement profiles for the Rangitaiki Fault at the seven interpreted horizons (Figure 9) show these five segments as well as three smaller faults (Ra-Rc) in the pseudo-3-D survey area. In general, the displacement of these faults decreases up section indicating synsedimentary growth faulting, and on each horizon the total displacement decreases from southwest to northeast. Individual fault segments are identified based on changes of fault displacement between adjacent segments and abrupt changes of strike.

[43] The southern most segment of the Rangitaiki Fault (R1) is 10 km long, accounting for half of the entire length of the Rangitaiki Fault (Figure 8). The southern tip of the R1 appears controlled, as discussed later, by the position of the volcanic Whale Island (Motuhora Island), an island that was formed before 450 ka (see *Burt et al.* [1996] for a review). The displacement profile of R1 is strongly asymmetric, with the maximum displacement only 2 km southwest of its northern tip. *Peacock and Sanderson* [1994] interpreted similar asymmetric profiles as resulting from overstepping fault segments linked by a relay ramp. Hence we infer that the asymmetric R1-R3 displacement profile is the result of the R2 relay between the two overlapping R1 and R3 segments. The transfer zone is imaged in both the high-resolution seismic reflection data and MCS reflection data; an example is shown in profile A-A′ (Figures 6 and 7). Most of the displacement in this profile is taken up on the transfer fault (R2), although R2 and R3 intersect at 1.4 s two-way time, so in deeper sediments the displacement must be accommodated solely by R1 and R3.

[44] North of the transfer zone, the intersecting antithetic faults Ra and Rb control the displacement profile of R3, from horizon MCS1 onward (Figure 9). At the line of intersection there is a decrease in displacement in R3 that matches the displacement at the intersecting tips of Ra (observed only in high-resolution data) and Rb. In the high-resolution data, Rc and R3 have complimentary displacement profiles; the drop in displacement in R3 is matched by the displacement of Rc. A similar example of fault complementarity is described by *Manighetti et al.* [2001].

[45] Northward, R3 connects with R4, and the rotation of the sediments in the ramp between the two interacting faults is most pronounced at horizon MCS1 (Figure 7, profile B-B′). R4 has distinct displacement profiles that divide the fault into segments R4a and R4b. From MCS1 onward, faults R4a and R4b appear linked, with only a small drop in displacement where they connect with fault R3 (Figures 9e–9g).

[46] R5 overlaps R4b, and continues to the northern tip of the Rangitaiki Fault. This segment is 5 km long and has a collapse graben in its hanging wall (Figures 5 and 7, profile C-C′). R5 continues northward beyond the pseudo-3-D survey area and terminates in a highly faulted area close to the White Island Fault.

6.3. Displacement Rates and Linkage History of the Rangitaiki Fault

[47] In Figure 10, the development of displacement on the faults at MCS3 is shown at five positions along strike, which correspond to the locations of the maximum displacement on segments R1, R3 R4a, R4b, and R5 in the pseudo-3-D survey area. Each of these graphs shows, from left to right, the increase in displacement on the segments from the deposition of MCS3 at 1340 ka to present. R3 shows the largest displacement recorded on MCS3 (Figure 9g), while the largest displacement on horizon HRS4 is recorded on R1 (Figure 9d). Location 1 (Figure 10, location 1) shows the development of the faults through the relay zone and in particular the late onset and subsequent rapid growth of fault R2. North of the transfer zone, at location 2, the displacement rate on fault R1 decreases and the displacement rate of R3 increases at 770 ka, i.e., after effective linkage of R1 and R3, to the south.

[48] Fault R3 changes in dip from its shallow dipping, high displacement center (4000–5000 m along strike) to a steeply dipping, low displacement northern section where it is overlaps fault R4a (5500–7000 m along strike). An important consequence of the variation in fault dip is the vertical changes in the structural relationships between the faults; for example, at horizon HRS4 the downthrown side of R3 is no longer colinear with the downthrown side of

Figure 8. (a) Map of the entire Rangitaiki Fault at horizon MCS1 (300 ± 100 ka). The main segments of the Rangitaiki Fault are numbered, the thickness of the fault represents the displacement as it varies along strike, and dots show fault tips. Other faults are in thinner solid lines. Bathymetry contours shown; there is a large surface expression of the White Island Fault. The rectangle shows the extent of the pseudo-3-D survey area; other fault displacement measurements are made from regional seismic lines (thin black lines) for MCS1 and from numerous 3.5 kHz, chirp, and boomer profiles (not shown) for HRS1. (b) Aggregate displacement profile for MCS1 with error bars (above hatched area in pseudo-3-D area) for the linked Rangitaiki Fault with the form of a single isolated fault and displacement lows at segment overlaps. The position of the detailed study area is shown. (c) Aggregate displacement profile for HRS1 with error bars (above hatched area in pseudo-3-D area) for the linked Rangitaiki Fault. The position of the detailed study area is shown; note that the MCS pseudo-3-D survey area is slightly offset from the HRS area. While the positions of the tips of the fault are well constrained, there is less control on displacement close to the tips (indicated by the dashed line).

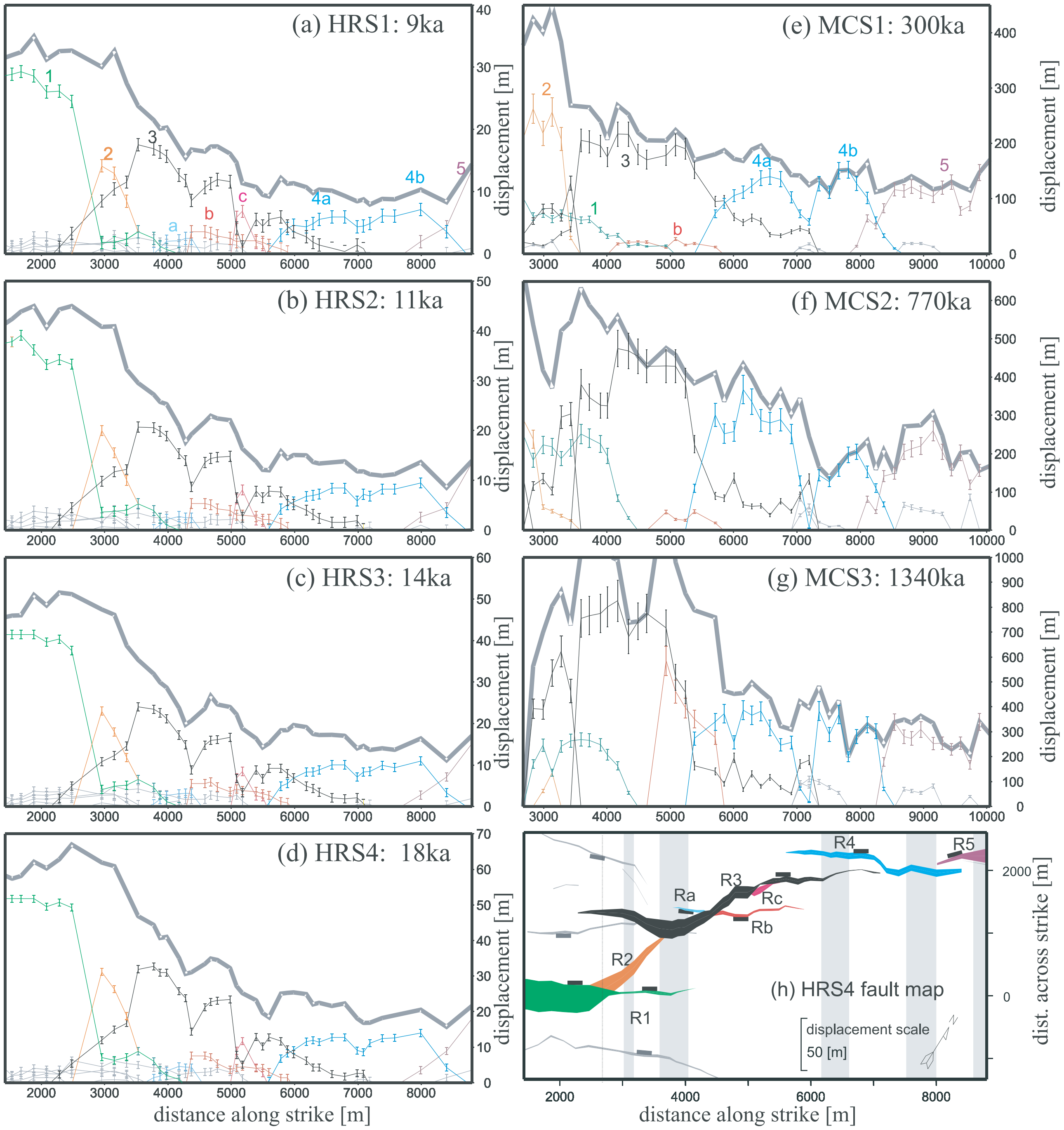

Figure 9. Profiles of total displacement on the Rangitaiki Fault measured on (a–d) four high-resolution and (e–g) three multichannel horizons within the 3-D box. (h) Displacement maps for horizon HRS4. The main segments of the Rangitaiki Fault are named and in color; the thick gray line shows the aggregate displacement profile for each horizon. See main text for a detailed discussion. Segment R1 continues south of the 3-D box (see Figure 8) but is not well imaged at HRS2-HRS4 levels on the high-resolution data or at MCS2 and MCS 3 levels in the multichannel seismic data.

R4a as it is at MCS3. Fault propagation and linkage of interacting faults can be inhibited or enhanced depending on their relative positions, so a change in fault geometry will alter the way the faults behave.

[49] Figure 11 shows the development of displacement on the Rangitaiki Fault from growth strata deposited above horizon MCS3. Figure 11 is produced by backstripping the displacements on the growth faults. R2 is not included in this analysis as its displacement profiles indicate that it has not behaved as a growth fault. The maximum displacement measured on R2 is found on horizon MCS1, and unlike the other faults in the pseudo-3-D survey area, the displacement decreases downward, suggesting a downward propagation of the fault.

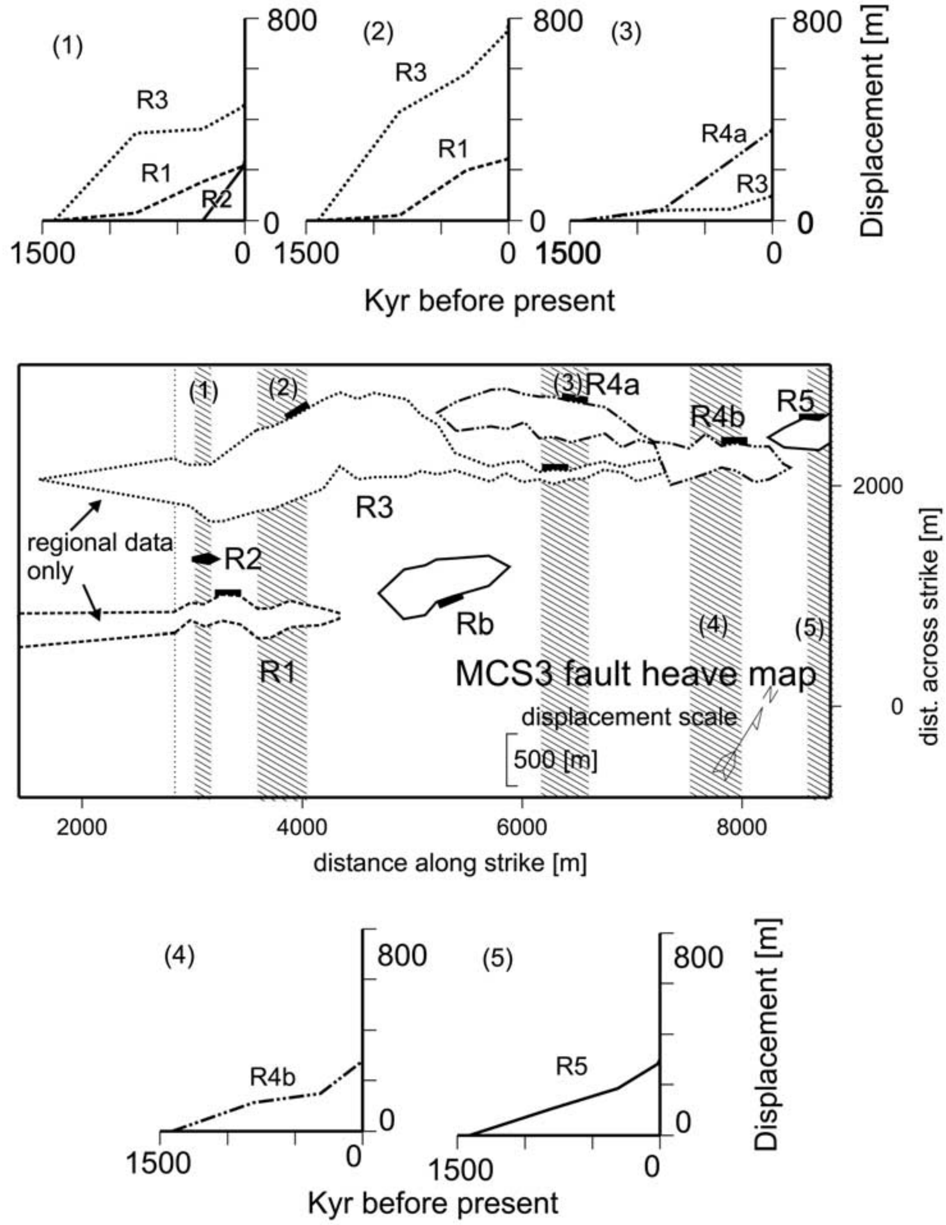

Figure 10. Displacement accumulation graphs corresponding to the maximum displacement locations of segments R2 (location 1 plot), R3 (location 2 plot), R4a (location 3 plot), R4b (location 4 plot) and R5 (location 5 plot) of the Rangitaiki Fault. Each plot shows the displacement accumulated on horizon MCS3 plotted against time in thousand years before present. Horizontal fault segments represent periods of fault quiescence; high gradients represent high displacement rates; displacement rate values for graphs 1–5 are given in Table 3. Displacement curves are plotted for each fault active at each location. The positions of and extent of data included in these plots are shown (hatched areas) in relation to a fault heave map of horizon MCS3. This map shows the horizontal separation of the upthrown and downthrown sides of the major Rangitaiki Fault segments R1 (dashed line), R2 (solid line), R3 (dotted line), R4 (dash-dotted line), and R5 (solid line).

[50] Fault R1 shows little or no displacement in the pseudo-3-D survey area between 1340 and 770 ka and then began accumulating displacement without showing any tip propagation between 300 ka and present. This suggests that R1 was present but inactive between 1340 and 770 ka or R1 propagated laterally at around 3 mm yr^{-1} northward. While R1 is propagating laterally (770–300 ka), the displacement rate on R3 is minimal with a value of 0.08 ± 0.08 mm yr^{-1} (Table 3), reduced from 0.60 mm yr^{-1} for the previous time period. Similarly, at location 2 the displacement rate of R3 decreases from 0.72 to 0.31 mm yr^{-1} as R1 propagates and overlaps R3. After the transfer fault R2 has linked R1 and R3, R1 ceases to propagate laterally, and all three faults are active at the same time, with R2 being the most active. After R1 and R3 are linked, their overlapping tips become relatively

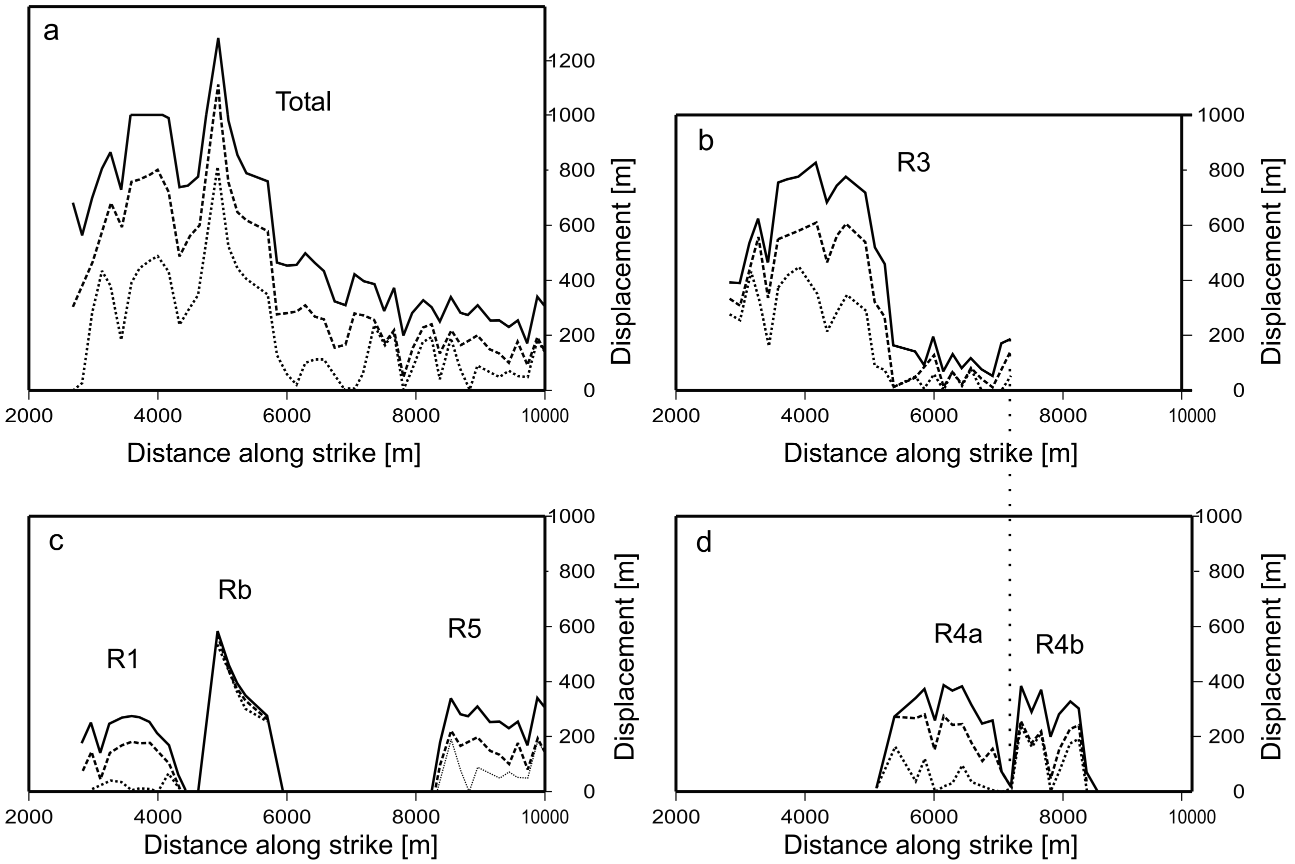

Figure 11. Displacement accumulation profiles for faults R1–R5 observed on horizon MCS3. (a) Total aggregate displacement profiles of the Rangitaiki Fault. (b–d) Individual profiles for segments R1–R5, shown separately for clarity. Present-day displacement profiles are shown by solid lines, displacement on horizon MCS3 backstripped to 300 ka values is shown by dashed lines, and displacement backstripped to 770 ka values is shown by dotted lines. The vertical dotted line linking Figures 11b and 11d indicates the position of linkage between R3, R4a, and R4b. The oblique transfer fault R2 is not shown as it formed only in the last 300 kyr.

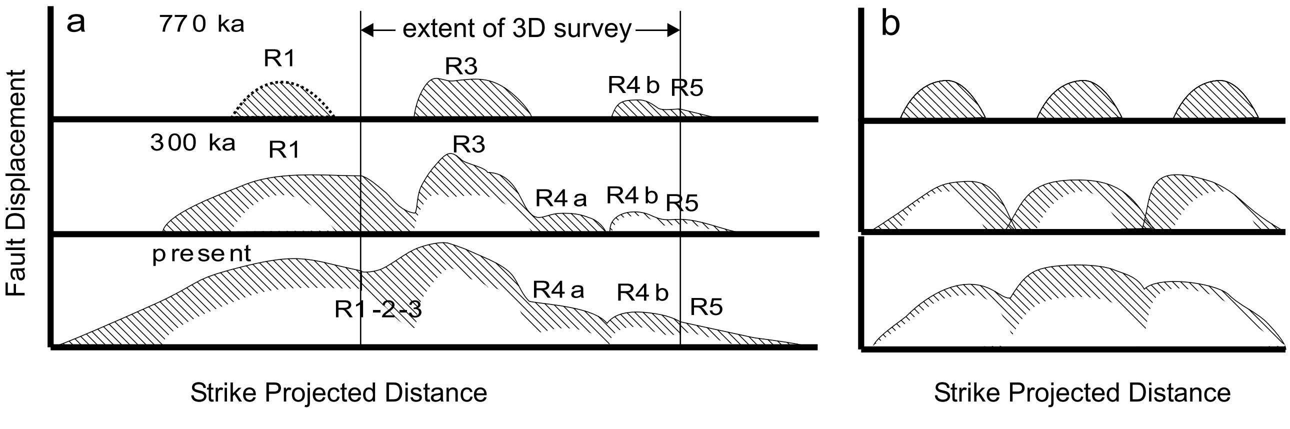

Figure 12. Schematic showing the temporal development of displacement on the entire Rangitaiki Fault system (a) as a strike projection of the oldest horizon (MCS3) within the detailed study area and (b) comparison with a model of tip propagation and linkage for normal faults proposed by *Cartwright et al.* [1995]. Hatched areas indicate where new displacement is accumulated in comparison to the previous time periods. The evolution from isolated faults to a fully linked system over 1.3 Myr is shown. The position of the southernmost segment of the Rangitaiki Fault, R1, is less well constrained for the earliest time period, and this is indicated by the dotted displacement profile.

Table 3. Fault Displacement Rates Determined Within the 3-D Box[a]

		Location 1			Location 2		Location 3		Location 4	Location 5
	Average	R1-max	R2	R3	R1	R3-max	R3	R4a-max	R4b	R5
1340-770 ka	0.52 ± 0.18	negligible	X	0.60 ± 0.24	negligible	0.72 ± 0.23	negligible	negligible	0.20 ± 0.13	0.19 ± 0.12
770-300 ka	0.47 ± 0.15	0.32 ± 0.14	X	0.08 ± 0.08	0.38 ± 0.13	0.31 ± 0.16	negligible	0.40 ± 0.17	negligible	0.18 ± 0.10
300-18 ka	0.75 ± 0.23	0.23 ± 0.10	0.79 ± 0.24	0.34 ± 0.13	0.17 ± 0.09	0.65 ± 0.20	0.18 ± 0.10	0.43 ± 0.15	0.45 ± 0.15	0.39 ± 0.14
18-0 ka	1.41 ± 0.31	0.37 ± 0.08	1.60 ± 0.36	0.75 ± 0.17	0.28 ± 0.06	1.76 ± 0.4	0.24 ± 0.05	0.66 ± 0.15	0.74 ± 0.17	1.01 ± 0.23

[a] Rates are in mm yr^{-1}, and rates quoted as "negligible" are below 0.10 mm yr^{-1} and have errors larger than the calculated rate. The calculation of average displacement rates for the entire fault system was determined by summing the aggregate strike-projected displacement rates and dividing by the number of observations (line crossings). Individual displacement rate observations are for the five locations shown in Figure 10.

inactive and accommodate a smaller proportion of the overall fault displacement (Figure 9d).

[51] The present-day displacement profile of R3 (heavy black line in Figure 11b) shows the fault has maximum displacement of 830 ± 130 m at ~4000 m along strike (location 2 in Figure 10 and Table 3) and a low displacement tail (<200 m) toward its northern tip. The northern tip of R3 has a nonzero displacement as it now intersects the center of R4 (Figure 11d). Backstripping the displacement on R3 shows that the position of the maximum displacement on the fault has not moved, and the fault has developed the low displacement tail between 300 ka and present, giving a timescale for the linkage of R3 and R4. Prior to linkage, segments R4a and R4b are alternately active, with negligible displacement rate on R4a and a maximum of 0.20 ± 13 mm yr^{-1} (Table 3 and Figure 10, locations 3 and 4) on R4b between 1340 and 770 ka and a maximum of 0.40 ± 0.17 mm yr^{-1} on R4a and negligible displacement rate on R4b between 770 and 300 ka. After linkage at 300 ka, the displacement rates on R4a and R4b are similar (0.43 ± 0.15 and 0.45 ± 0.15 mm yr^{-1}, Table 3). The current displacement profiles (Figure 9) show that the intersection point between R4a and R4b has its maximum displacement at horizon MCS1 (Figure 9e). Assuming that the linkage initiated at or near the surface, these observations suggest that R4a and R4b linked at ~300 ka, forming a kinematically coherent fault segment, R4. This linkage occurred at approximately the same time as, and may have been driven by, the linkage of R3 with these faults.

[52] The heave map in Figure 10 shows that the hanging wall cutoff of R3 is approximately colinear with the hanging wall cutoff of fault 4a at horizon MCS3, which is no longer the case at younger horizons (Figure 9). The backstripped displacement profiles for the earliest observable time on the seismic sections (Figure 11d) shows R4a has virtually no displacement except at the southeastern tip. This active tip of R4a may be the continuation of R3 along strike at this horizon. This colinear relationship is not preserved up section because the faults are slightly curved and have variable dip along strike. We infer that the damage caused by the propagation of R3 and its eventual linkage with R4 was what initiated the linkage between R4a and R4b.

[53] The total displacement across R4 to R5 has a flat-topped profile, i.e., the aggregate displacement profile shows no significant decrease across the overlap (Figure 9). *Childs et al.* [1993] interpreted similar flat-topped profiles, as observed in sandbox analogue models, to be a result of upward propagation of a single large fault. These faults step over only 200 m, a small distance compared with their lengths of between 3 and 5 km (compare >1 km offset between R2 and R3). The fault displacement rates are in phase throughout their history (Table 3 and Figure 10, locations 4 and 5). This fault interaction history is interpreted as the result of tip line bifurcation [*Huggins et al.*, 1995; *Childs et al.*, 1996], where the vertical propagation of the tip line is locally retarded by heterogeneity in the rock.

[54] Figure 11c shows that Rb accumulates very little displacement after 770 ka; this is inferred to be as a result of the southeast dipping Rb connecting with the dominant northwest dipping segments of the Rangitaiki Fault and becoming locked. The five main segments of the Rangitaiki Fault network all dip toward the northwest; fault Rb, however, dips toward the southeast. The opposing dips of faults R3 and Rb cause their relative positions to change on each successive horizon [*Childs et al.*, 1995] until they eventually connect at horizon MCS1. The effect of the intersection is seen in the displacement profiles of horizon MCS1 (Figure 9e), where the southern tip of Rb (4000 m along strike) coincides with a drop in displacement in R3. The relationship between these faults is further changed up section as both the faults become steeper toward the seabed until they are both close to vertical. Where both faults are vertical, the slip vectors of the faults are in the same orientation, and both faults may remain active [*Jackson and McKenzie*, 1983]. A consequence of this is that displacement may be transferred across fault R3. This transfer of displacement results in the continuation of fault Rb across R3, forming fault Ra (Figures 9a–9d). *Nicol et al.* [1995] found a reduction in displacement on discrete faults and a corresponding increase in ductile strain at the seismic scale. The data presented here agree with this result, as total displacement for the Rangitaiki Fault system shows a drop in displacement around the intersection point. In all the horizons where Ra is observed, its displacement is less than the displacement of Rb at the intersection (Figures 9a–9d). This is interpreted to be because only Rb is driving the displacement on Ra from seismogenic depths (Ra is not observed any deeper than HRS4) and the transfer of displacement across R3 also involves transfer of displacement onto subseismic-scale faults.

7. Discussion

[55] The above observations enable us to make the following interpretation of the evolution of the Rangitaiki Fault.

7.1. Fault Evolution

[56] These data (Figures 11 and 12) show the development of a fault network from isolated faults to a fully linked structure, initially by tip propagation followed by the development of relay zones and their subsequent breaching.

The imaging of horizon MCS3, which formed early (1.3 Ma) in the development of the rift, ensures that the entire history of fault growth can be determined. The total displacement accumulated over the last ~20 kyr (i.e., displacement profile on HRS4, Figure 9d) resembles an isolated fault with maximum displacement near the center tapering to zero at the tips, suggesting that over long timescales (tens of thousands of years) the entire Rangitaiki Fault is now behaving as a single fault structure, from seismogenic depths (~6 km [*Bryan et al.*, 1999]) to the surface. The displacement profiles of MCS2 and MCS3 reflect displacements accumulated both when the Rangitaiki Fault behaved as a single fault and when the Rangitaiki Fault comprised isolated and laterally propagating faults. The combination of fault growth regimes results in distorted displacement profiles at MCS2 and MCS3 and large displacement gradients at segment boundaries (Figures 9f and 9g).

[57] The evolution of the fault system from isolated faults to a fully linked network is summarized in sections 7.1.1 to 7.1.4.

7.1.1. From 1340 to 770 ka: Isolated Fault Segments

[58] Within the pseudo-3-D survey area, the Rangitaiki Fault comprised five short, isolated faults dipping both to the northwest and the southeast. The active segments were R3 (at this time resolvable as two separate fault segments), R4b, R5, and Rb. R1 was not active within the survey area at this time, although regional seismic profiles show it to be active within 1–2 km to the south (Figure 12). We cannot identify the active length of R1 at this time because we have not been able to identify MCS3 and MCS2 along the southern part of R1. The deformation is limited to a 1.5-km-wide deformation band, with an average displacement rate of 0.52 ± 0.18 mm yr^{-1}. The maximum displacement rate of an isolated segment (R3-max, Table 3) is 0.72 ± 0.23 mm yr^{-1}. The Rangitaiki Fault is dominantly growing at this time through the processes of fault nucleation and tip propagation, comparable with the early rift initiation stage described by *Cowie et al.* [2000].

7.1.2. From 770 to 300 ka: Early Fault Interaction

[59] At this stage the faults were beginning to overlap and interact but with no increase in overall displacement rate (Table 3). The average displacement rate on the Rangitaiki Fault at this time was 0.47 ± 0.15 mm yr^{-1}. All the displacement was taken up on northwest dipping faults, as the antithetic fault Rb is not active at this time (Figures 9f and 11c). Activity on faults Rb and R4b is negligible, and the two segments of R3 that were identified in the older sediments must have linked, as they are indistinguishable at this level. The northern tip of R3 has propagated laterally and overlaps R4a by 600 m. R1 propagated into the survey area and overlapped R3 by nearly 2 km. R4a ceased to be colinear with R3 and was offset by ~500 m.

7.1.3. From 300 to 18 ka: Fault Interaction and Linkage

[60] During this time fault linkage became an important process in the development of the fault network, and the Rangitaiki Fault became a fully linked system (Figure 11a). The average displacement rate on the whole system almost doubled to 0.72 ± 0.23 mm yr^{1}. The five linked segments produce a continuous fault of total length ~20 km (Figure 12).

[61] The relay ramp between overlapping faults R1 and R3 was breached by the development of the oblique transfer fault R2. The development of the newly linked fault network was accompanied by increased displacement rates on, and lateral propagation of R1. R1 now has a length of ~10 km; approximately half the length of the linked fault system (Figure 8). Faults R3, R4a and R4b also linked at this time, and R4 began to behave as a single fault with a displacement low remaining at the intersection with the tip of R3.

7.1.4. From 18 ka to Present: Fully Linked Fault Network

[62] Throughout the last 18 kyr the Rangitaiki Fault has been a fully linked fault system (Figure 12). The overlapping tips of R1 and R3 are now relatively inactive. R4 is well developed as a single structure, with evidence for the previous segmentation remaining only as a minor displacement low in the center of the displacement profile. The average displacement rate of the Rangitaiki Fault network has increased through time from its initial rate of 0.52 ± 0.18 mm yr^{-1} initially, when the faults were isolated, to 1.41 ± 0.31 mm yr^{-1} in the fully linked network. The maximum aggregate displacement rate recorded over the last 18 kyr is 3.4 ± 0.2 mm yr^{-1} at ~2500 m along strike. Note that the location of maximum displacement has shifted southward relative to previous time periods, with an aggregate displacement rate of 2.72 ± 0.61 mm yr^{-1} at location 1 (Table 3).

7.2. Implications for Fault Growth Models

[63] Fault propagation is inherently a three-dimensional process, and it is important to discuss the relative roles of both vertical and lateral components of propagation through the brittle seismogenic crust. The base of the seismogenic zone beneath the Taupo Volcanic Zone can be defined as the depth above which 80% of the earthquakes occur [*Smith and Bruhn*, 1984], and for the study area this is at 6 km [*Bryan et al.*, 1999], or by consideration of the modeling results of the Edgecumbe earthquake (see discussion by *Beanland et al.* [1990]), which suggest that brittle deformation could continue to 8 km depth. Therefore the thickness of the seismogenic zone in the nearshore Whakatane Graben is likely to be in the range of 6–8 km. While it is clear that the Rangitaiki Fault system became hard linked between 300 and 18 ka, consideration must be given as to whether the segments of the Rangitaiki Fault were kinematically independent structures which linked late, or whether they grew and evolved as part of one kinematically coherent fault array from early in their development. Backstripping displacement shows that the horizontal separation of fault R3 from R4 and R5 is greater than 2 km during the period 1340 and 770 ka. In addition, R1 was certainly offset from R3 by at least this distance at this time (although R1 is not well imaged at these earlier periods). Given this separation, and the relative thinness of the seismogenic zone, it can be argued that, R1, R3, and R5 were unlinked at all seismogenic depths. However, *Nicol et al.* [1996] noted that close to the upper tip line of normal faults, displacement contours are typically subhorizontal and fault propagation is inferred to be subvertical. Nicol et al. argue that growth faults form in association with mainly upward propagation near to the free surface, where maps of these faults show a significant component of out-of-plane propagation [see also *Walsh et al.*, 2003]. As discussed earlier the evolution of segments R4 and R5 is interpreted to be due to the vertical propaga-

tion of a single fault at depth. The development of fault segments R1, R3, and R5 by upward bifurcation and propagation of a deeper main fault cannot be excluded given the limited depth extent of the available seismic data. Nevertheless, we believe that the development of faulting is best explained by a series of faults (R1, R3, and R5) forming in isolation early in the development of the Whakatane Graben, with upward propagation forming R4-R5 and R2 forming as a late stage oblique transfer fault. Further deeper seismic data are required to test this interpretation.

[64] *Manighetti et al.* [2001] in an analysis of active normal faults in Afar, argued that changes with time in the position of maximum displacement could be interpreted in terms of the direction of propagation of the fault system. Manigheti et al. also discussed the role of initiation points where slip starts and barriers where fault propagation is arrested. Data presented here (Figure 11) suggest that once displacement resolvable by our MCS data is accumulated on a fault segment, the position of the maximum displacement on that segment does not change with time. Furthermore the position of maximum aggregate displacement, which is close to the center of the linked fault array (Figure 11a), has not moved during the last 1.3 Myr. The southern tip of the Rangitaiki Fault system abuts against Whale Island and it is likely that this has inhibited further southward propagation of the system. The distribution of recent displacement (Figures 8c and 12a, bottom) shows the displacement gradient being higher toward the more southerly barrier, and a lower displacement gradient toward the northern end where the Rangitaiki Fault system is interacting with the White Island Fault (Figure 1) and perhaps still propagating northward. While these displacement gradient results are consistent with the model proposed by *Manighetti et al.* [2001], they can also be explained as resulting from overstepping fault segments linked by a relay ramp [*Peacock and Sanderson*, 1994] as discussed earlier. Discrimination between these alternative explanations requires the analysis of displacement length data for many more faults, which is the subject of continuing work focused on high-resolution imaging of HRS4 (J. M. Bull et al., manuscript in preparation, 2004).

[65] The youthfulness of the Rangitaiki Fault system, together with our stratigraphic resolution, means that we are able to document the full history of fault evolution. Unlike previous studies [e.g., *Nicol et al.*, 1997] we are able to resolve the earliest stages of fault evolution. We show that displacement rates are relatively slow during the earliest history of fault growth (the first ~1 Myr) and that there is a threefold increase in the displacement rate of the linked fault system in comparison with the unlinked system. In common with the analogue models of *Mansfield and Cartwright* [2001], there is considerable spatial variability in displacement rate between segments in both the linked and unlinked fault systems as relict boundaries still remain significant barriers to displacement accumulation. In addition, the reliance on discrete stratigraphic markers will undoubtedly hide complexity in the temporal changes in slip rates (for discussion of the intrinsic variability of slip rates, see *McCalpin* [1995]).

[66] Comparison of the threefold increase in displacement rate observed during the development of a fully linked system for the Rangitaiki Fault with other fault systems is hampered by insufficient temporal and spatial resolution in previously published work. One of the few documented examples of displacement rate increase caused by fault linkage is found in the northern North Sea. *McLeod et al.* [2000] found a fault displacement rate increase from 0.055 to 0.092 mm yr^{-1} in the Strathspey-Brent-Statfjord fault associated with a major phase of fault linkage. This linkage event occurred between 10 and 14 Ma after rift initiation [*McLeod et al.*, 2000].

[67] On the Rangitaiki Fault, where displacement rates are ~8 times faster than in the North Sea, interaction and linkage become the dominant processes only after ~1 Ma of fault activity, again approximately eight times faster than in the North Sea setting seen by *McLeod et al.* [2000]. Although these displacement rate changes and linkage events are happening on different timescales and length scales, the simple scaling of rates of displacement and rates of linkage are suggestive that the same process is responsible for each, and is happening at different scales.

[68] Localization of strain onto major throughgoing fault structures is often accompanied by a corresponding decrease in activity on surrounding faults [*McLeod et al.*, 2000; *Meyer et al.*, 2002] such that the overall strain rate for the region may remain constant [*Gupta et al.*, 1998]. The pseudo-3-D survey area was selected to document the development of the Rangitaiki Fault system, and does not include a representative sample of regional faulting. Because of this it cannot show conclusively whether the recorded increase in displacement rate on the linked fault system is at the expense of displacement accumulation on adjacent faults. However, the seismic profile interpreted by *Davey et al.* [1995] does show a concentration of recent TVZ fault activity in the eastern Whakatane Graben, including the Rangitaiki Fault. Considering the deformation of the whole TVZ permits the constraint of constant regional strain rate to be satisfied without demanding the faults immediately adjacent to the Rangitaiki Fault decrease in activity. Figure 12 shows a schematic of the evolution of the entire Rangitaiki Fault system, and a comparison with a model of tip growth and linkage proposed by *Cartwright et al.* [1995]. The position of R1 at the earliest time period is less well constrained, but it is clear that the segments R1, R3, and R4b-R5 were isolated faults. The segments propagated toward each other, initially with high displacement gradients at their segment tips. Between 300 and 18 ka the system linked and displacement accumulated on segments with a reduction in displacement gradient within the linked system. The displacement rates on segments of the Rangitaiki Fault are such that the linked array displacement profile approximates to an idealized isolated fault. Displacement rates on individual fault segments are highly variable along strike, and are influenced more by interactions with neighboring faults and their location within the linked system than by their initial length. In this paper we have demonstrated that the broad conceptual idea of fault growth by tip growth and segment linkage is correct, but also show how displacement rates and displacement gradients evolve over the entire history of fault growth.

8. Conclusions

[69] In this paper we have investigated the complete evolution of the most active fault system within the

Whakatane Graben, the Rangitaiki Fault. The fault initiated as isolated segments, which grew together over 1 Myr. Fault tip propagation was the dominant faulting process initially (from 1340 to 770 ka), followed by the development of relay zones and their subsequent breaching. The system became fully linked between 300 and 18 ka. Because of the stratigraphic range and resolution of our seismic reflection data sets, and the youthfulness of the fault system, we are able to show that the average displacement rate (0.52 ± 0.18 mm yr^{-1}) was relatively low during the earlier (unlinked) stages of fault growth. Following linkage, the average displacement rate of the fault system increased threefold in comparison to the unlinked array, to 1.41 ± 0.31 mm yr^{-1}. The maximum displacement rate changed from 0.72 ± 0.23 mm yr^{-1} for an isolated segment (R3) to an aggregate 3.4 ± 0.2 mm yr^{-1} for the linked array.

[70] The displacement profile of the fully linked Rangitaiki Fault resembles that of a single fault, whereas displacement profiles of horizons deposited before the faults linked are irregular and have strong displacement gradients on the fault segments. More generally, we show that displacement profiles derived from offsets on horizons formed early in a fault system's evolution will exhibit complex displacement profiles due to the superposition of processes operating when the system operated as a single fault, and when its constituent segments were isolated and laterally propagating.

[71] **Acknowledgments.** This work was funded by the Natural Environment Research Council (GR3/11862 and Tied Studentship to S.K.T.), United Kingdom, and the New Zealand Foundation for Research Science and Technology (FRST-CO1X0038). We are grateful to the officers and crew of R/V *Tangaroa* and R/V *Kaharoa* for their dedication during TAN-99-14 and KAH01-02 and to Justin Dix and the technical team at NIWA for their expertise in geophysical data acquisition. We thank the following for their biostratigraphic input: Tony Edwards (Stratigraphic Solutions) and Graeme Wilson, Dallas Mildenhall, and Percy Strong (Institute of Geological and Nuclear Sciences). Dave Sanderson, Patience Cowie, and Ian Wright are thanked for their support and helpful comments. Isabelle Manighetti, Andy Nicol, and the Associate Editor Iain Stewart provided thorough and constructive reviews which improved the final manuscript.

References

Beanland, S., and K. R. Berryman (1992), Holocene coastal evolution in a continental rift setting; Bay of Plenty, New Zealand, *Quat. Int.*, *15/16*, 151–158.

Beanland, S., G. H. Blick, and D. J. Darby (1990), Normal faulting in a back-arc basin: Geological and geodetic characteristics of the 1987 Edgecumbe earthquake, New Zealand, *J. Geophys. Res.*, *95*, 4693–4707.

Best, A. I., and D. E. Gunn (1999), Calibration of marine sediment core loggers for quantitative acoustic impedance studies, *Mar. Geol.*, *160*, 137–146.

Bryan, C. J., S. Sherburn, H. M. Bibby, S. C. Bannister, and A. W. Hurst (1999), Shallow seismicity of the central Taupo Volcano Zone, New Zealand: Its distribution and nature, *N. Z. J. Geol. Geophys.*, *42*, 533–542.

Burgmann, R., D. D. Pollard, and S. J. Martel (1994), Slip distributions on faults: Effects of stress gradients, inelastic deformation, heterogeneous host-rock stiffness, and fault interaction, *J. Struct. Geol.*, *16*, 1675–1690.

Burt, R. M., J. W. Cole, and P. Z. Vroon (1996), Volcanic geology and geochemistry of Motuhora (Whale Island), Bay of Plenty, New Zealand, *N. Z. J. Geol. Geophys.*, *39*, 565–580.

Carter, R. M., L. Carter, and D. P. Johnson (1986), Submergent shorelines, SW Pacific: Episodic post-glacial transgression, *Sedimentology*, *33*, 629–649.

Cartwright, J. A., B. D. Trudgill, and C. S. Mansfield (1995), Fault growth by segment linkage: And explanation for scatter in maximum displacement and trace length data from the Canyonlands Grabens of SE Utah, *J. Struct. Geol.*, *17*, 1319–1326.

Cartwright, J. A., C. S. Mansfield, and B. D. Trudgill (1996), The growth of faults by segment linkage, in *Modern Developments in Structural Interpretation, Validation and Modelling*, edited by P. G. Buchanan and D. A. Nieuwland, *Geol. Soc. Spec. Publ.*, *99*, 163–177.

Chapman, T. J., and A. W. Meneilly (1991), The displacement patterns associated with a reverse-reactivated, normal growth fault, in *The Geometry of Normal Faults*, edited by A. M. Roberts, G. Yielding, and B. Freeman, *Geol. Soc. Spec. Publ.*, *56*, 183–191.

Childs, C., S. J. Easton, B. C. Vendeville, M. P. A. Jackson, S. T. Lin, J. J. Walsh, and J. Watterson (1993), Kinematic analysis of faults in a physical model of growth faulting above a viscous salt analogue, *Tectonophysics*, *228*, 313–329.

Childs, C., J. Watterson, and J. J. Walsh (1995), Fault overlap zones within developing normal fault systems, *J. Geol. Soc. London*, *152*, 535–549.

Childs, C., J. Watterson, and J. J. Walsh (1996), A model for the structure and development of fault zones, *J. Geol. Soc. London*, *153*, 337–340.

Cowie, P. A., and C. H. Scholz (1992a), Physical explanation for displacement-length relationship for faults using a post-yield fracture mechanics model, *J. Struct. Geol.*, *14*, 1133–1148.

Cowie, P. A., and C. H. Scholz (1992b), Growth of faults by accumulation of seismic slip, *J. Geophys. Res.*, *97*, 11,085–11,096.

Cowie, P. A., S. Gupta, and N. H. Dawers (2000), Implications of fault array evolution for synrift depocentre development: Insights from a numerical fault growth model, *Basin Res.*, *12*, 241–261.

Darby, D. J., K. M. Hodgkinson, and G. H. Blick (2000), Geodetic measurement of deformation in the Taupo Volcanic Zone, New Zealand: The north Taupo network revisited, *N. Z. J. Geol. Geophys.*, *43*, 157–170.

Davey, F. J., and E. Lodolo (1995), Crustal seismic study of and Ensialic Back-Arc Basin (Bay of Plenty) New Zealand, *Boll. Geofis. Teor. Appl.*, *37*, 25–37.

Davey, F. J., S. A. Henrys, and E. Lodolo (1995), Asymmetric rifting in a continental back-arc environment, North Island, New Zealand, *J. Volcanol. Geotherm. Res.*, *68*, 209–238.

Dawers, N. H., M. H. Anders, and C. H. Scholz (1993), Growth of normal faults: Displacement-length scaling, *Geology*, *21*, 1107–1110.

De Mets, C., R. G. Gordon, D. F. Argus, and S. Stein (1994), Effect of recent revisions to the geomagnetic reversal time scale on estimates of current plate motions, *Geophys. Res. Lett.*, *21*, 2191–2194.

Froggatt, P. C., and D. J. Lowe (1990), A review of late Quaternary silicic and some other tephra formations from New Zealand: Their stratigraphy, nomenclature, distribution, volume and age, *N. Z. J. Geol. Geophys.*, *33*, 89–109.

Gibb, J. G. (1986), A New Zealand regional Holocene eustatic sea-level curve and its application to determination of vertical tectonic movements. A contribution to IGCP- Project 200, *Bull. R. Soc. N. Z.*, *24*, 377–395.

Gupta, S., P. A. Cowie, N. H. Dawers, and J. R. Underhill (1998), A mechanism to explain rift-basin subsidence and stratigraphic patterns through fault-array evolution, *Geology*, *26*, 595–598.

Herzer, R. H. (1981), Late Quaternary stratigraphy and sedimentation of the Canterbury continental shelf, New Zealand, *N. Z. Oceanogr. Inst. Mem.*, *89*, 71 pp.

Houghton, B. F., C. J. N. Wilson, M. O. McWilliams, M. A. Lanphere, S. D. Weaver, R. M. Briggs, and M. S. Pringle (1995), Chronology and dynamics of a large silicic magmatic system: Central Taupo Volcanic Zone, New Zealand, *Geology*, *23*, 13–16.

Huggins, P., J. Watterson, J. J. Walsh, and C. Childs (1995), Relay zone geometry and displacement transfer between normal faults recorded in cola-mine plans, *J. Struct. Geol.*, *17*, 1741–1755.

Jackson, J., and D. McKenzie (1983), The geometrical evolution of normal fault systems, *J. Struct. Geol.*, *5*, 471–482.

Kohn, B. P., and G. P. Glasby (1978), Tephra distribution and sedimentation rates in the Bay of Plenty, New Zealand, *N. Z. J. Geol. Geophys.*, *21*, 49–70.

Lamarche, G., P. M. Barnes, J. M. Bull, R. Garlick, A. Hill, H. Horgan, J. Mitchell, S. K. Taylor, and S. Wilcox (1999), Tan99-14 cruise report: Bay of Plenty neotectonics, internal report, Natl. Inst. of Water and Atmos. Res., Wellington, New Zealand.

Lamarche, G., J. M. Bull, P. M. Barnes, S. K. Taylor, and H. Horgan (2000), Constraining fault growth rates and fault evolution in New Zealand, *Eos Trans. AGU*, *81*, 481, 485–486.

Lambeck, K., and J. Chappell (2001), Sea level change through the last glacial cycle, *Science*, *292*, 679–686.

Manighetti, I., G. C. P. King, Y. Gaudemer, C. Scholz, and C. Doubre (2001), Slip accumulation and lateral propagation of active normal faults in Afar, *J. Geophys. Res.*, *106*, 13,667–13,696.

Mansfield, C. S., and J. A. Cartwright (1996), High-resolution displacement mapping from three-dimensional seismic data: Evidence for dip linkage during fault growth, *J. Struct. Geol.*, *18*, 249–263.

Mansfield, C. S., and J. A. Cartwright (2001), Fault growth by linkage and implications from analogue models, *J. Struct. Geol.*, *23*, 745–763.

McCalpin, J. P. (1995), Frequency distribution of geologically determined slip rates for normal faults in the western United States, *Bull. Seismol. Soc. Am.*, *85*, 1867–1872.

McLeod, A. E., N. H. Dawers, and J. R. Underhill (2000), The propagation and linkage of normal faults: Insights from the Strathspey-Brent-Statfjord fault array, northern North Sea, *Basin Res.*, *12*, 263–284.

Meyer, V., A. Nicol, C. Childs, J. J. Walsh, and J. Watterson (2002), Progressive localisation of strain during the evolution of a normal fault population, *J. Struct. Geol.*, *24*, 1215–1231.

Nairn, I. A., and S. Beanland (1989), Geological setting of the 1987 Edgecumbe earthquake, New Zealand, *N. Z. J. Geol. Geophys.*, *32*, 1–13.

Nicol, A., J. J. Walsh, J. Watterson, and P. Bretan (1995), The three-dimensional geometry and growth of conjugate normal faults, *J. Struct. Geol.*, *17*, 847–862.

Nicol, A., J. Watterson, J. J. Walsh, and C. Childs (1996), The shapes, major axis orientations and displacement patterns of fault surfaces, *J. Struct. Geol.*, *18*, 235–248.

Nicol, A., J. J. Walsh, J. Watterson, and J. R. Underhill (1997), Displacement rates on normal faults, *Nature*, *390*, 157–159.

Pascouet, A. (1991), Something new under the water: The bubbleless air gun, *Leading Edge*, *10*(11), 79–81.

Peacock, D. C. P., and D. J. Sanderson (1991), Displacement, segment linkage and relay ramps in normal fault zones, *J. Struct. Geol.*, *13*, 721–733.

Peacock, D. C. P., and D. J. Sanderson (1994), Geometry and development of relay ramps in normal fault systems, *AAPG Bull.*, *78*, 147–165.

Peacock, D. C. P., R. J. Knipe, and D. J. Sanderson (2000), Glossary of normal faults, *J. Struct. Geol.*, *22*, 291–305.

Pollard, D. D., and P. Segall (1987), Theoretical displacements and stresses near fractures in rock: With applications to faults, joints, veins, dikes, and solution surfaces, in *Fracture Mechanics of Rock*, edited by B. K. Atkinson, pp. 277–350, Academic, San Diego, Calif.

Sclater, J. G., and P. A. F. Christie (1980), Continental stretching: An explanation of the post-mid-cretaceous subsidence of the central North Sea basin, *J. Geophys. Res.*, *85*, 3711–3739.

Smith, R. B., and R. L. Bruhn (1984), Intraplate extensional tectonics of the eastern Basin Range: Inferences on structural style from seismic reflection data, regional tectonics, and thermo-mechanical models of brittle-ductile deformation, *J. Geophys. Res.*, *89*, 5733–5762.

Thore, P., A. Shtuka, M. Lecour, T. Ait-Ettajer, and R. Cognot (2002), Structural uncertainties: Determination, management, and applications, *Geophysics*, *67*, 840–852.

Trudgill, B. D., and J. A. Cartwright (1994), Relay ramp forms and normal fault linkages: Canyonlands National Park, Utah, *Geol. Soc. Am. Bull.*, *106*, 1143–1157.

Walcott, R. I. (1978), Present tectonics and late Cenozoic evolution of New Zealand, *Geophys. J. R. Astron. Soc.*, *52*, 137–164.

Walcott, R. I. (1984), The kinematics of the plate boundary zone through New Zealand: A comparison of short and long-term deformations, *Geophys. J. Int.*, *79*, 613–633.

Walcott, R. I. (1987), Geodetic strain and the deformational history of the North Island of New Zealand during the late Cainozoic, *Philos. Trans. R. Soc. London, Ser. A*, *321*, 163–181.

Walsh, J. J., and J. Waterson (1988), Analysis of the relationship between displacements and dimensions of faults, *J. Struct. Geol.*, *10*, 239–247.

Walsh, J. J., W. R. Bailey, C. Childs, A. Nicol, and C. G. Bonson (2003), Formation of segmented normal faults: A 3-D perspective, *J. Struct. Geol.*, *25*, 1251–1262.

Wright, I. C. (1990), Late Quaternary faulting of the offshore Whakatane Graben, Taupo Volcanic Zone, New Zealand, *N. Z. J. Geol. Geophys.*, *33*, 245–256.

Wright, I. C. (1992), Shallow structure and active tectonism of an offshore continental back-arc system: The Taupo Volcanic Zone, New Zealand, *Mar. Geol.*, *103*, 287–309.

Wu, D., and R. L. Bruhn (1994), Geometry and kinematics of active normal faults, South Oquirrh Mountains, Utah: Implications for fault growth, *J. Struct. Geol.*, *16*, 1061–1075.

P. M. Barnes and G. Lamarche, National Institute of Water and Atmospheric Research, 301 Evans Bay Parade, Greta Point, P.O. Box 14-901, Kilbirnie, Wellington, New Zealand. (p.barnes@niwa.co.nz; g.lamarche@niwa.co.nz)

J. M. Bull, School of Ocean and Earth Science, Southampton Oceanography Centre, Southampton SO14 3ZH, UK. (bull@soton.ac.uk)

S. K. Taylor, Fault Analysis Group, Department of Geology, University College Dublin, Dublin 4, Ireland. (susanna@fag.ucd.ie)